



Norwegian University of  
Science and Technology

Lithium ion conductivity and phase  
composition of  $3\text{Li}_2\text{S} + \text{P}_2\text{S}_5 - 2\text{LiBH}_4 +$   
 $\text{LiBr}$  composites.

**Astrid Bygdås Høgset**

Master of Science in Physics and Mathematics

Submission date: June 2018

Supervisor: Ragnvald H. Mathiesen, IFY

Co-supervisor: Magnus Sørby, Institutt for energiteknikk

Norwegian University of Science and Technology  
Department of Physics



---

# Abstract

The crystal structure and electrochemical properties of a mixed  $\text{LiBH}_4\text{-LiBr-Li}_2\text{S-P}_2\text{S}_5$  system have been studied, with the aim to investigate relations between ionic conductivity and sample content, and to evaluate the materials electrochemical properties. Five samples with different concentration rates were synthesized by ball milling and annealing, and the crystalline phases were determined by powder X-ray diffraction, powder neutron diffraction and infrared spectroscopy. The ionic conductivities were decided by electrochemical impedance spectroscopy, and electrochemical properties were investigated through battery tests and cyclic voltammetry.

Impedance measurements showed ionic conductivities in the range  $10^{-4}$  -  $10^{-3}$  S  $\text{cm}^{-1}$  at room temperature, thus the materials are classified as superionic conductors. X-ray diffraction displayed that  $\text{Li}_6\text{PS}_5\text{Br}$  had been formed in all samples after synthesizing, while  $\text{Li}(\text{BH}_4)_{1-y}\text{Br}_y$  was present in three out of the samples. It has previously been reported that the positions and the amount of substituted bromide in the structures effect how local ionic diffusivity translates to macroscopic ionic conductivity, and several structural features have been investigated in order to find a relation between crystal content and measured conductivities. It was however not possible to find an absolute correlation.

Concerning the structure of  $\text{LB}_{0.33}\text{LPS}_{0.67}$ , the structure model fitted to the X-ray diffraction data did not match with the neutron diffractogram. A new structure model of the  $\text{Li}_6\text{PS}_5\text{Br}$  phase was therefore introduced, including the possibility of borohydride substitution in the structure. The new model gave a better fit for both diffractograms, thus it is suggested that borohydride can be substituted into the argyrodite structure of  $\text{Li}_{7-x-y}\text{PS}_{6-x-y}\text{Br}_x(\text{BH}_4)_y$ .

---

Battery cycling of the  $\text{LB}_{0.33}\text{LPS}_{0.67}$  sample showed repeatable cyclability at  $\frac{C}{20}$  and good stability towards the electrode material at 323 K, indicating that the material displays promising properties as electrolyte material.

---

# Samandrag

Dette studiet tek føre seg krystallstrukturen og dei elektrokjemiske eigenskapane til eit sett av prøver frå eit blanda system av  $\text{LiBH}_4\text{-LiBr-Li}_2\text{S-P}_2\text{S}_5$ , der målet har vore å finne ein samanheng mellom ioneleiingsevna og strukturen av prøvene, samt å kartlegge materiala sine elektrokjemiske eigenskapar. Kulemølling og varmebehandling var brukt til å syntetisere fem prøver av ulike konsentrasjonsmengder. Krystallstrukturen av prøvene vart kartlagt ved hjelp av pulver røntgen-pulverdiffraksjon, nøytron-pulverdiffraksjon og infraraud spektroskopi. Konduktiviteten til materiala blei studert ved hjelp av elektrokjemisk impedans-spektroskopi, og dei elektrokjemiske eigenskapane til prøvene vart studert gjennom syklisk voltammetri og batterisykling.

Impedansmålingane viste at leiingsevna til materiala ligg i området  $10^{-4} - 10^{-3} \text{ S cm}^{-1}$  ved romtemperatur, og materiala kan derfor kategoriserast som gode ioneleiarar. Resultata frå røntgendiffraksjon viste at  $\text{Li}_6\text{PS}_5\text{Br}$  har blitt danna i alle prøvene, medan  $\text{Li}(\text{BH}_4)_{1-y}\text{Br}_y$  har blitt danna i tre av dei fem prøvene. Det har tidlegare blitt vist at både posisjonen og mengda av substituert brom i strukturane har innverknad på korleis den lokale diffusiviteten av ionane påverkar den makroskopiske leiingsevna til materiala. Ulike strukturelle eigenskapar har difor blitt studert i eit forsøk på å finne ein samanheng mellom leiingsevne og material struktur, men det har ikkje lykkast i å finne ein absolutt korrelasjon. Strukturmodellen som vart nytta ved Rietveld forfiningane av  $\text{LB}_{0.33}\text{LPS}_{0.67}$  ved røntgendiffraksjon passa ikkje med dei observerte data frå nøytrondiffraksjon av same prøve. Med bakgrunn i dette vart ein ny strukturmodell introdusert, kor også borhydrid kunne substituerast inn i krystallstrukturen. Den nye strukturmodellen korrelerte godt med diffraktogramma frå både nøytron- og røntgendiffraksjon, og det er difor

---

foreslått at også borhydrid kan substituerast inn i argyrodite strukturen av  $\text{Li}_{7-x-y}\text{PS}_{6-x-y}\text{Br}_x(\text{BH}_4)_y$ .

Batteritestar utført med  $\text{LB}_{0.33}\text{LPS}_{0.67}$  som elektrolyttmateriale viste repetativ sykling ved syklingsrate  $\frac{C}{20}$ , og god stabilitet mot elektrodematerialet ved 323 K. Dette indikerer at materialet har lovande eigenskapar som elektrolyttmateriale.

---

# Contents

<b>1</b>	<b>Introduction</b>	<b>9</b>
<b>2</b>	<b>Theory</b>	<b>11</b>
2.1	Solid state battery . . . . .	11
2.1.1	Ionic conductivity . . . . .	13
2.2	Electrochemical impedance spectroscopy . . . . .	15
2.3	Crystal structure . . . . .	17
2.4	X-ray Diffraction . . . . .	20
2.5	Neutron diffraction . . . . .	24
2.6	Rietveld refinement . . . . .	25
2.7	Infrared Spectroscopy . . . . .	27
2.8	Symmetry and vibrational modes . . . . .	28
<b>3</b>	<b>Experimental methods</b>	<b>31</b>
3.1	Sample preparation . . . . .	31
3.2	Powder X-ray diffraction . . . . .	32
3.2.1	X-ray diffraction, home lab . . . . .	32
3.2.2	Synchrotron radiation . . . . .	33
3.3	Powder neutron diffraction . . . . .	34
3.4	Electrochemical Impedance Spectroscopy . . . . .	35
3.5	Cyclic voltammetry . . . . .	36
3.6	Cell assembly . . . . .	38
3.7	Infrared Spectroscopy . . . . .	39
3.8	Differential Scanning Calorimetry . . . . .	39
<b>4</b>	<b>Results</b>	<b>41</b>
4.1	Impedance measurements . . . . .	42

## CONTENTS

---

4.2	Structural analysis . . . . .	47
4.2.1	Powder X-ray diffraction . . . . .	47
4.2.2	Infrared spectroscopy . . . . .	56
4.2.3	Powder neutron diffraction . . . . .	59
4.3	Analysis of $\text{LB}_x\text{LPS}_{1-x}$ as electrolyte material . . . . .	62
4.3.1	Thermal stability . . . . .	62
4.3.2	Electrochemical stability . . . . .	64
4.3.3	Battery test . . . . .	66
<b>5</b>	<b>Discussion</b>	<b>69</b>
5.1	Conductivity and structure . . . . .	69
5.2	$\text{LB}_x\text{LPS}_{(1-x)}$ as electrolyte material . . . . .	72
5.3	Further work . . . . .	73
<b>6</b>	<b>Conclusion</b>	<b>75</b>
	<b>Bibliography</b>	<b>77</b>
<b>A</b>	<b>Impedance measurements</b>	<b>81</b>
A.1	Uncertainty in the impedance measurements . . . . .	81
A.2	Nyquist plots of all samples . . . . .	82
<b>B</b>	<b>Structural analysis</b>	<b>85</b>
B.1	Infrared spectroscopy . . . . .	85
B.1.1	$\text{LiBH}_4$ . . . . .	85
B.1.2	LB . . . . .	87
B.2	Powder X-ray diffraction . . . . .	88
B.2.1	Stabilization of HT- $\text{LiBH}_4$ by halide substitution	88
B.3	Powder neutron diffraction . . . . .	91
B.3.1	Misfit of structure model . . . . .	91
B.3.2	Difference in PND sample and SR-PXD sample .	93
B.3.3	Neutron diffraction of LPS sample . . . . .	94
<b>C</b>	<b>Properties for electrolyte materials</b>	<b>95</b>
C.1	Thermal analyses . . . . .	95
C.1.1	Diffraction of heat treated $\text{LB}_{0.25}\text{LPS}_{0.75}$ . . .	95
C.1.2	TGA . . . . .	97
C.2	Cycling of $\text{LB}_{0.50}\text{LPS}_{0.50}$ . . . . .	97



---

# Preface

This thesis presents the work conducted during the final semester of the Master in Science program in Physics and Mathematics at the Norwegian University of Science and Technology. The thesis is a collaboration between NTNU, Institutt for fysikk, and IFE, Institutt for Energiteknikk, and it presents some of the ongoing research that is carried out at IFE.

I would like to express my gratitude to Magnus Sørby, my main supervisor at IFE, for valuable guidance, feedback and for always being optimistic and present. Secondly, I would like to thank Ragnvald Mathiesen, my supervisor at NTNU, for sharing of his vast knowledge and for valuable and thorough feedback. Lastly, I would like to express my gratitude for the opportunity to write my thesis in such an appreciative environment as IFE.

*CONTENTS*

---

# Chapter 1

---

## Introduction

Lithium ion batteries are considered to be among the best options for energy storage in a vast selection of appliances. Compared to other secondary batteries, they have displayed higher energy densities, higher cell voltage, lower self-discharge rate, quicker charge acceptance and better cycle life. An extensive drawback with the conventional lithium ion battery is that it utilizes flammable organic solvents as electrolyte material, which introduces considerable safety issues. By exchanging the combustible liquid electrolyte with a non-flammable solid electrolyte, safety issues related to both mechanical stress, fire hazards and leakage can be omitted. However, solid electrolytes suffers from challenges due to insufficient ionic conductivities at room temperature and difficulties in forming an effective electrode-electrolyte interface. To overcome these issues, and to realize the all solid-state battery, it is important to understand both the internal processes of the battery and the material properties of the components.

Lithium borohydride,  $\text{LiBH}_4$ , is a crystalline material which undergoes a structural transition from an orthorhombic phase (LT) to a hexagonal phase (HT) at approximately 390 K, where the HT-phase exhibits high ionic conductivity [1]. It has been shown that the  $\text{BH}_4^-$  anion can be chemically substituted by  $\text{Cl}^-$ ,  $\text{Br}^-$  and  $\text{I}^-$  halides, which lead to room temperature stabilization of the HT-phase [2].  $\text{LiBH}_4$  is regarded as a good candidate for use in solid electrolytes, as it obtains high ionic conductivity, high stability against a lithium metal electrode and low grain

---

boundary resistance [3].

Several lithium sulfide compounds have displayed both high ionic conductivities and showed promising electrochemical properties for use in solid state batteries. One of the sulfide electrolytes that have been intensively investigated is  $\text{Li}_2\text{S-P}_2\text{S}_5$ , which exhibit conductivity values in the order of  $10^{-4} \text{ S cm}^{-1}$  at room temperature [4].

The effect of mixing  $\text{LiBH}_4$  and  $\text{Li}_2\text{S-P}_2\text{S}_5$  have previously been studied by Yamauchi *et al* [5], where it was found that the mixed materials obtained higher conductivity values than the starting material. This was explained by the fact that  $\text{LiBH}_4$  had been incorporated into the amorphous sulfide, and the state of the incorporated  $\text{BH}_4^-$  anions was similar to that of  $\text{BH}_4^-$  ions in HT- $\text{LiBH}_4$ . A similar study was continued by Unemoto *et al* [6] by combining  $\text{LiBH}_4$  with  $\text{Li}_2\text{S}$  and  $\text{P}_2\text{S}_5$  in different concentrations. In their work, the resultant materials were not amorphous, but a new complex hydride-sulphide crystalline phase was found.

By mixing orthorhombic  $\text{LiBH}_4$  with  $\text{Li}_2\text{S}$  and  $\text{P}_2\text{S}_5$ , Yamauchi *et al* and Unemoto *et al* obtained materials with increased conductivities compared to the starting materials. It is known that the ionic conductivity of hexagonal  $\text{LiBH}_4$  are several orders of magnitude higher than orthorhombic  $\text{LiBH}_4$ . It was therefore of interest to study how the same system of mixed materials would perform by utilizing the hexagonal phase of  $\text{LiBH}_4$  instead of the orthorhombic.

The work presented in this thesis is thus based on an equivalent system, expanded with addition of  $\text{LiBr}$ ,  $(3\text{Li}_2\text{S} + \text{P}_2\text{S}_5) + (2\text{LiBH}_4 + \text{LiBr})$ . A total of five mixed samples have been synthesized, and the relationship between the sample content and the material's conductivities has been investigated, as well as their electrochemical properties.

# Chapter 2

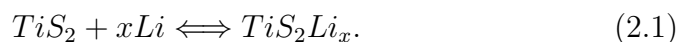
---

## Theory

### 2.1 Solid state battery

A battery converts chemical energy to electrical energy via redox reactions inside the battery cell. The electrons involved in the reactions are forced to move in an outer circuit, which enables them to be used as a power source. A vast variety of batteries exist, and this study will focus exclusively on lithium ion solid-state batteries.

The main components in a solid-state battery cell is illustrated in figure 2.1. During the discharge of the battery, lithium atoms are oxidized at the anode, and migrate to the cathode through the electrolyte. The electrons are collected at the current collector, and transferred to the cathode via an external circuit. At the cathode, the lithium ions are reduced, and lithium atoms are intercalated between layers of titaniumdisulfide. The reactions are reversed when the battery is charged, and the total cell reaction is given as



The current of the battery is decided from the concentration of the lithium-ions involved in the lithiation and delithiation process.

## 2.1. SOLID STATE BATTERY

---

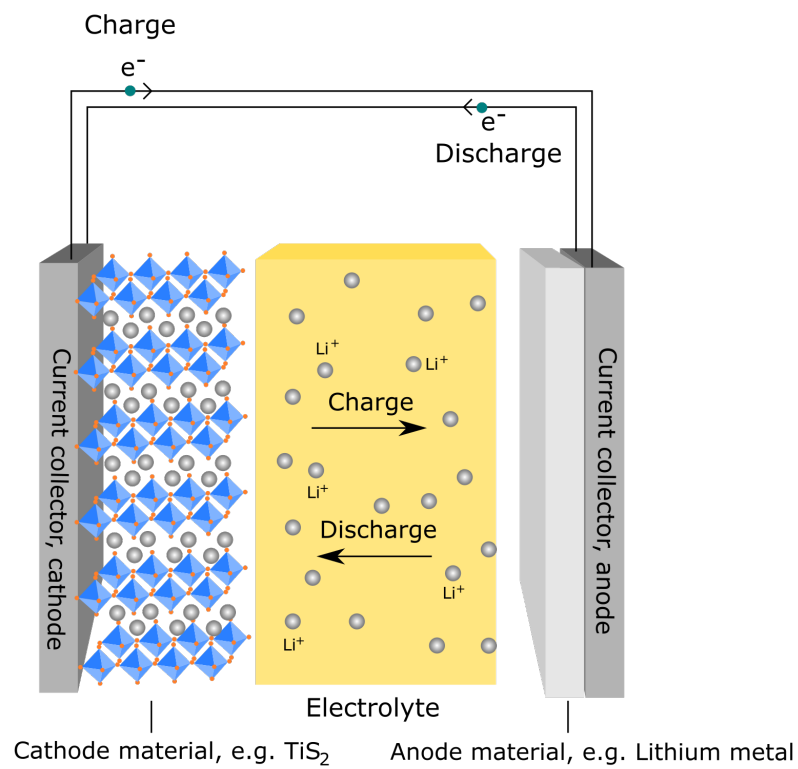


Figure 2.1: Illustration of a lithium ion solid state battery. The lithium ions propagate through the electrolyte, while the electrons are forced to move in an outer circuit.

### 2.1.1 Ionic conductivity

The atomic movements in solids are normally mediated by structural defects, and figure 2.2 illustrates how atoms can move in the crystalline lattice. The vacancy mechanism, where an atom moves to a vacant site, is the most common. Atomic diffusion in solids is driven by the concentration gradient of impurity atoms, vacancies or interstitials, and is quantified through the diffusion coefficient. The diffusion coefficient is proportional to the net flux of atoms in the material and the concentration gradient driving the diffusion. The ionic conductivity and atomic diffusivity result from the same macroscopic transport mechanisms, but the ionic conductivity is characterized by a non-zero mean displacement,  $\langle x \rangle$ , and the diffusivity a non-zero mean-square displacement  $\langle x^2 \rangle$ . The relation between conductivity and diffusivity is given as

$$\frac{\sigma_A}{D_A} = \frac{n_A q_A^2}{k_B T}, \quad (2.2)$$

where  $\sigma_A$  is the conductivity,  $D_A$  diffusivity,  $n_A$  is the number of ions,  $q_A$  is the ionic charge,  $k_B$  is the Boltzmann's constant, and  $T$  the temperature.

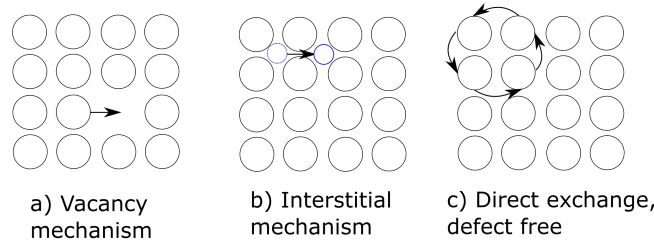


Figure 2.2: Illustration of possible atomic movement in crystal structure.

The diffusion coefficient is temperature dependent, as it requires thermal energy to transfer an atom from one site to another and to create the defects. The energy required to create a defect is given by the Gibbs free energy

$$\Delta g_f = \Delta h_f - T \Delta s_f, \quad (2.3)$$

## 2.1. SOLID STATE BATTERY

---

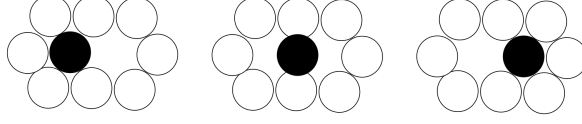


Figure 2.3: An atom moving from one site to another has to overcome an energy barrier to intervene atoms in the structure.

where  $\Delta h_f$  is the enthalpy,  $\Delta s_f$  the entropy and  $T$  the temperature. An atom moving from one site to another has to overcome an energy barrier to intervene atoms in the structure, illustrated in figure 2.3. This barrier is equal to the activation free energy for atomic mobility, and is given as

$$\Delta g_m = \Delta h_m - T\Delta s_m, \quad (2.4)$$

where  $\Delta h_m$  is the enthalpy,  $\Delta s_m$  the entropy.

The atoms travel through the crystal via a series of discrete jumps over the activation barriers, and the diffusion is therefore influenced by both the probability of finding neighboring defects and the jump frequency of the atom. The probability of finding a neighboring defect (e.g. a vacancy) is given as  $p = e^{-\frac{\Delta g_f}{k_b T}}$ . The jump frequency is given as the product of the atomic vibrational frequency,  $\nu_A$ , and the probability of making a jump,  $\gamma_A = \nu_A \cdot e^{-\frac{\Delta g_m}{k_b T}}$ .

These relations combined with equation (2.2) gives the temperature dependence of the ionic conductivity

$$\sigma_A T = A \cdot e^{-\frac{E_D}{k_b T}}, \quad (2.5)$$

where  $E_D$  is the conductivity activation energy,  $E_D = \Delta h_f + \Delta h_m$ .  $A$  is given as  $\frac{f_c a^2 \nu_A n_A q_A^2}{6} \cdot \exp\frac{\Delta s_f + \Delta s_m}{k_b}$ , where  $a$  is the jump distance and  $f_c$  is a proportionality constant.

Thus, the conductivity activation energy can be found from the slope of  $\ln(\sigma T)$  as function of  $T^{-1}$  [7] [8].



## 2.2 Electrochemical impedance spectroscopy

The principle of electrochemical impedance spectroscopy (EIS) is to apply a frequency dependent voltage signal,  $\Delta V \cdot e^{j\omega t}$  to a cell, and measure the current response,  $\Delta I \cdot e^{j\omega t - \phi}$ , where  $\phi$  is the phase difference. The frequency dependent impedance is then given as

$$Z(\omega) = \frac{\Delta \cdot e^{j\omega t}}{\Delta I \cdot e^{j\omega t - \phi}} = \frac{\Delta V}{\Delta I} (\cos(\phi) + i \sin(\phi))$$

The phase shift, and thereby the impedance, depends on the electrochemical processes in the system. The impedance is often graphically represented in Nyquist plots, where the real part of the impedance is plotted on the x-axis and the imaginary part on the y-axis. By calculating the equivalent circuit representation of the Nyquist plots, kinetic processes can be represented by combinations of resistances, capacitances and inductances in parallel and series. Because the kinetic processes inside the material have different time constants, one can separate and investigate different contributions to the total impedance by probing the system over a wide range of frequencies.

The Simplified Randle circuit describes the basic processes present in every cell, and is therefore a good starting point for more complex models. It consists of a resistance in series with a parallel combination of a capacitor and a resistor, illustrated in figure 2.4. The resistor  $R_1$  represents the solution resistance,  $R_2$  the charge transfer resistance and  $C$  the double layer capacitance at the electrode/electrolyte interface.<sup>1</sup> When a high-frequency signal is applied to the circuit, the capacitor will function as a wire, which enables quantification of  $R_1$ . By applying a low-frequency signal,  $R_1$  and  $R_2$  will act as resistors in series, and  $R_2$  is easily calculated. The capacitance is calculated by applying the relation

$$\omega_{max} = \frac{1}{RC} \quad (2.6)$$

to the extracted values at the maximum point of the semicircle, illustrated in 2.4. The calculated capacitance values gives the domain of which the feature is attributed to, described in table 2.1 [9, 10, 11, 12].

<sup>1</sup>On the interface between the electrode and the electrolyte there will be formed two layers of ions with opposing polarity when a voltage is applied.

## 2.2. ELECTROCHEMICAL IMPEDANCE SPECTROSCOPY

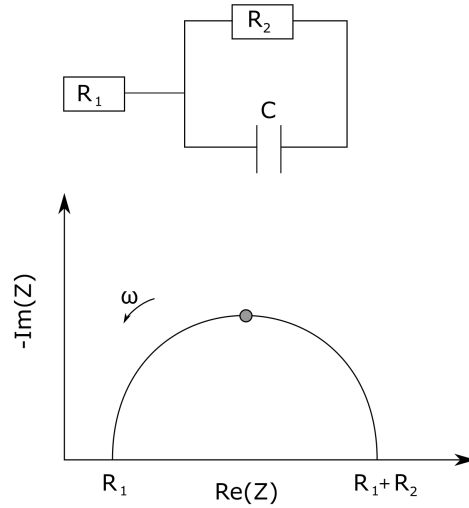


Figure 2.4: The figure illustrates both the simplified Randles cell, top, and the Nyquist plot, bottom, for the same circuit. The Nyquist plot for the simplified Randles cell is always a semicircle. The solution resistance,  $R_1$ , can be read off at the high frequency intersection with the real axis, which is in the left part of the plot. The diameter of the semicircle gives the value for  $R_2$ . The capacitance,  $C$ , can be calculated by extracting the impedance and frequency at the point marked at the top of the semicircle, and using equation 2.6.

Capacitance [F]	Phenomenon responsible
$10^{-12}$	Bulk
$10^{-11} - 10^{-8}$	Grain Boundary
$10^{-7} - 10^{-5}$	Sample-electrode interface
$10^{-4}$	Electrochemical reactions

Table 2.1: Capacitance values and some of the possible interpretations, [9]

## 2.3 Crystal structure

Solid materials are classified into categories in terms of atomic structure. Crystals have some form of long range order in their atomic arrangement, whereas amorphous materials only possess short range order.

A single crystal is a three dimensional periodic arrangement of atoms, ions or molecules. The crystal can be represented by a lattice, which consists of lattice points that have identical surroundings. The lattice points are translationally repeated in a periodic fashion in all vector directions.

In an infinite lattice with points having the same translational periodicity as the crystal, one can uniquely express the distance between two lattice points in terms of three translation vectors,  $\mathbf{a}_1$ ,  $\mathbf{a}_2$ , and  $\mathbf{a}_3$ , as

$$\mathbf{R} = u\mathbf{a}_1 + v\mathbf{a}_2 + w\mathbf{a}_3, \quad (2.7)$$

where  $u$ ,  $v$  and  $w$  are integers. The primitive unit cell is defined as the volume in which encloses a single lattice point, and it is spanned by the primitive translational vectors. The total volume of the crystal is spanned by translation operations of the primitive unit cell volume.

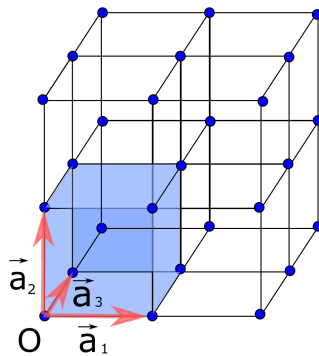


Figure 2.5: Unit cell with lattice vectors.

By permuting all possible 3D combinations of symmetry operations, and dividing them into classes that impose the same restrictions due to their cell parameters, 7 crystal systems are obtained. Combining the seven crystal systems with the four possible types of centering gives 14 different crystal lattices. These are called the Bravais lattices, and are

### 2.3. CRYSTAL STRUCTURE

---

shown in figure 2.6. In total, 230 different space group symmetries may be realized within the 14 Bravais lattices.

The periodically repeated unit in the lattice is called the basis, and is constituted either by atoms, ions or molecular units. A crystal is fully described by the symmetry operations of its space group and its basis.

The reciprocal lattice represents the Fourier transform of the Bravais lattice. In the same way as for the crystal lattice, the distance between two reciprocal lattice points for a three dimensional crystal can be determined by

$$\underline{\mathbf{h}} = h\mathbf{a}_1^* + k\mathbf{a}_2^* + l\mathbf{a}_3^*, \quad (2.8)$$

where  $\mathbf{a}_1^*$ ,  $\mathbf{a}_2^*$ ,  $\mathbf{a}_3^*$  are reciprocal lattice vectors, and h,k and l are integers referred to as Miller indices. The reciprocal lattice vectors are defined by

$$\mathbf{a}_i^* = 2\pi \frac{\mathbf{a}_j \times \mathbf{a}_k}{\mathbf{a}_i \cdot (\mathbf{a}_j \times \mathbf{a}_k)}, \quad \mathbf{a}_i \cdot \mathbf{a}_j^* = \delta_{i,j}. \quad (2.9)$$

The reciprocal lattice and the direct lattice belong to the same crystal system, and thus have the same translational and symmetry operations.

A lattice plane of the Bravais lattice is defined as a plane of which the intersections with the lattice are periodic, illustrated in figure 2.7. The planes, referred to as hkl-planes, can be described using the Miller indices, which are inversely proportional to the axial cross sections  $x_1$ ,  $x_2$ ,  $x_3$  of the lattice vectors;

$$h : k : l = \frac{1}{x_1} : \frac{1}{x_2} : \frac{1}{x_3}. \quad (2.10)$$

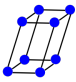
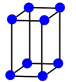
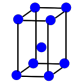
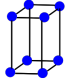
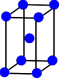
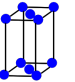
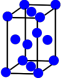
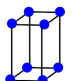
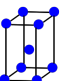
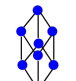
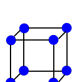
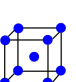
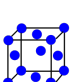

Bravais lattice	Parameters	Simple	Volume centered	Base centered	Phase centered
Triclinic	$a_1 \neq a_2 \neq a_3$ $\alpha_{12} \neq \alpha_{23} \neq \alpha_{31}$				
Monoclinic	$a_1 \neq a_2 \neq a_3$ $\alpha_{23} = \alpha_{31} = 90$ $\alpha_{12} \neq 90$				
Ortho rhombic	$a_1 \neq a_2 \neq a_3$ $\alpha_{12} = \alpha_{23} = \alpha_{31} = 90$				
Tetragonal	$a_1 = a_2 \neq a_3$ $\alpha_{12} = \alpha_{23} = \alpha_{31} = 90$				
Trigonal	$a_1 = a_2 = a_3$ $\alpha_{12} = \alpha_{23} = \alpha_{31} < 120$				
Cubic	$a_1 = a_2 = a_3$ $\alpha_{12} = \alpha_{23} = \alpha_{31} = 90$				
Hexagonal	$a_1 = a_2 \neq a_3$ $\alpha_{12} = 120$ $\alpha_{23} = \alpha_{31} = 90$				

Figure 2.6: The 14 Bravais lattices.

## 2.4. X-RAY DIFFRACTION

---

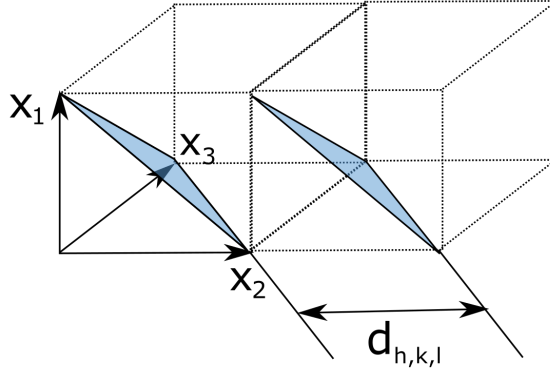


Figure 2.7: The figure illustrates the repetitive planes. In this case the  $[1,1,1]$  plane is shown, and  $d_{h,k,l}$  is the distance between the planes.

The reciprocal lattice vectors are normal to the lattice planes, and can thus be used to find the distances,  $d_{h,k,l}$  between neighboring planes in the crystal, [8, 13, 14]

$$d_{hkl} = \frac{2\pi}{|\underline{\mathbf{h}}|}. \quad (2.11)$$

## 2.4 X-ray Diffraction

When a crystal is exposed to an X-ray beam, the oscillating field from the electromagnetic waves will force the atomically bound electron to oscillate with the same frequency as the electric field of the wave. The oscillating electron is accelerated with the spatiotemporal variations of the electric field, and will emit electromagnetic radiation in all directions. If there are no energy loss during the interaction, the resultant wave will have the same frequency and wavelength as the incoming wave. If the incident X-ray beam is monochromatized, the waves will be scattered with the same wavelength, and waves scattered by different atoms will interact by adding their amplitudes into a diffraction signal [13].

The scattering vector,  $\mathbf{K}$  is given as the difference between the incident beam with wave vector  $\mathbf{k}$  and the diffracted beam with wave vector  $\mathbf{k}'$ ,

$$\mathbf{K} = \mathbf{k}' - \mathbf{k}. \quad (2.12)$$

In the case of elastic scattering, there are no energy exchange between the wave and the scattering object, and hence no momentum transfer;  $|\mathbf{k}| = |\mathbf{k}'| = \frac{2\pi}{\lambda}$ , where  $\lambda$  is the wavelength. For constructive interference to occur, the overall phase factor must be equal to unity, which gives Laue's interference condition;

$$e^{i\mathbf{K}\mathbf{R}} = 1. \quad (2.13)$$

This is only satisfied when the scattering vector  $\mathbf{K}$  is equal to the reciprocal lattice vector  $\mathbf{h}$

$$\mathbf{K} = \mathbf{h}. \quad (2.14)$$

By combining equations 2.14 and 2.11, Braggs law can be derived,

$$2d \cdot \sin\theta = n\lambda, \quad (2.15)$$

where the scattering of the X-rays are regarded as specular reflections from the lattice planes.

The Ewald sphere is a geometric representation of the Laue interference condition. It is constructed by drawing the incoming wave vector  $\mathbf{k}$  so that it terminates at a reciprocal lattice point, which represents (0,0,0). A sphere with radius  $|\mathbf{k}| = \frac{2\pi}{\lambda}$  is drawn around the origin of the incoming wave vector  $\mathbf{k}$ , as shown in figure 2.8. If the Ewald sphere intersects with any other reciprocal lattice point, then  $\mathbf{k}' = \mathbf{k} + \mathbf{h}$ , thus Laue's interferes condition is satisfied and a diffracted beam will exist.

An ideal powder is composed of a high number of small crystallites with random orientations. Because the particles can take any orientation, the total reciprocal space representation of the powder will consist of a set of spherical surfaces with radius  $|\underline{h}|$  about 000, rather than discrete points. As a result, the intersection between the reciprocal lattices and the Ewald sphere will form rings where the interference condition is being satisfied, as illustrated in figure 2.8 and 2.9.

## 2.4. X-RAY DIFFRACTION

---

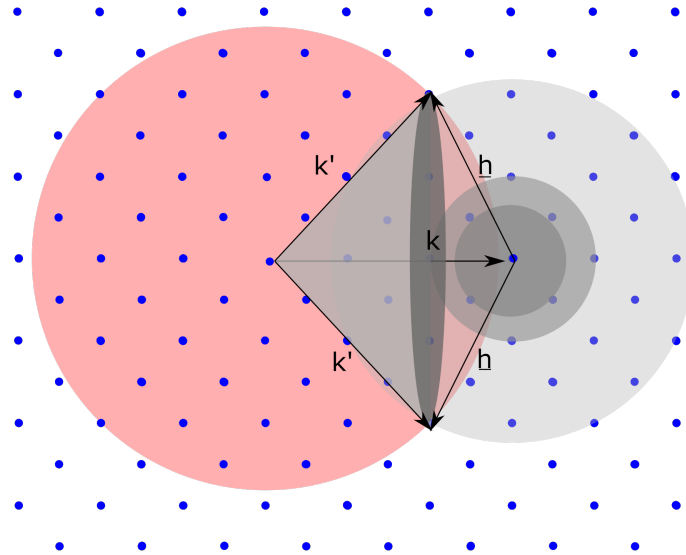


Figure 2.8: The Ewald sphere, illustrated in red, is constructed around the incoming wave vector,  $\mathbf{k}$ , and the scattering wave vector,  $\mathbf{k}'$ , as shown in this picture. The total reciprocal space representation of the powder will consist of a set of spherical surfaces with radius  $|h|$  about 000, illustrated by the grey spheres. The intersection between the reciprocal lattices and the Ewald sphere will form rings where the interference condition is being satisfied, illustrated in dark grey.



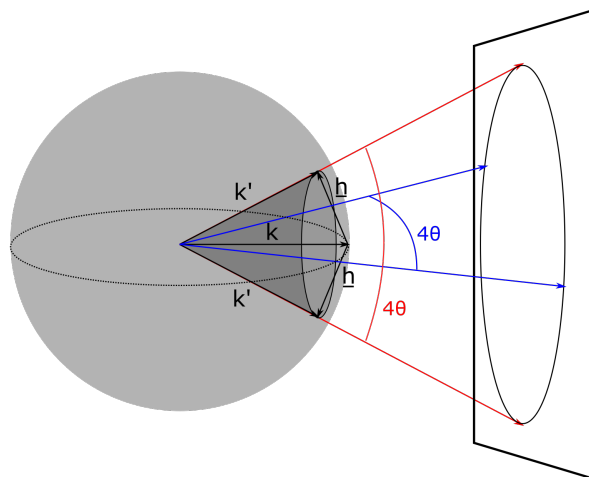


Figure 2.9: The intersections between the Ewald sphere and the total reciprocal space representation of the powder produces powder diffraction cones and the corresponding Debye ring on the screen/detector, as illustrated in the figure

The information about the atomic arrangement lies in the intensities of the Bragg peaks of Miller indices  $(hkl)$ ,  $I_{\underline{h}}$ . The observed intensities are proportional to the squared modulus of the structure factor  $F_{\underline{h}}$ , which describes both the amplitude and the phase of a Bragg reflection with indices  $hkl$ , and is given as

$$\mathbf{F}_{\underline{h}} = |F_{\underline{h}}|e^{i\phi_{\underline{h}}} = \sum_j f_j e^{i\mathbf{h}\mathbf{R}_j} \quad (2.16)$$

where  $|F_{\underline{h}}|$  is the amplitude,  $e^{i\phi_{\underline{h}}}$  the phase factor,  $f_j$  is the atomic scattering factor and the sum goes over all atoms  $j$  in the basis. The atoms and ions have electrons distributed around their nucleus, and their positions can be described by a probability distribution given by their quantum mechanical wave functions. The wave functions consist of radial functions and spherical harmonics, but by assuming spherical symmetry, the atomic form factor can be treated as the Fourier transform of the radial electron density distribution of the atom,

$$f_{\underline{h}} = \int \rho(\mathbf{r}) e^{i\underline{h} \cdot \mathbf{r}} d^3\mathbf{r}. \quad (2.17)$$

As the intensity is proportional to the squared modulus of the structure factor, it can be written as  $I_{\underline{h}} \propto \mathbf{F}_{\underline{h}} \cdot \mathbf{F}_{\underline{h}}^* = |F_{\underline{h}}|^2 \cdot e^{i\phi_{\underline{h}}} \cdot e^{-i\phi_{\underline{h}}} = |F_{\underline{h}}|^2$ , which shows that information about the phase is lost. This is known as the "Phase problem", and can be solved by dedicated methods [8, 14].

## 2.5 Neutron diffraction

Neutrons have no charge, and will therefore mainly interact with the atomic nuclei when they pass through matter. An exception is if the atoms contain unpaired electrons, as the neutron has a magnetic moment. The nuclear forces between the incoming neutron and the nucleus are short ranged, and the size of the scattering center is around 100 000 times smaller than the distance between the scatterers. Because of this, the neutron will experience solid matter as mostly empty void, and it can travel large distances through most materials without being scattered or absorbed.

According to quantum mechanics and the deBroglie equation, all particles with a linear moment also have a wavelength. A parallel beam of neutrons can thus be described by a plane wave. The wavelengths of thermal neutrons are comparable to the interatomic distances in materials, which enables diffraction from the structures.

As the neutron wavelengths are typically 4-5 orders of magnitude larger than the dimensions of the nucleus, the nucleus will scatter as a point source when a neutron interacts with an atomic nucleus. The atomic scattering factor, equation (2.17), is given as the Fourier transform of the spatial density function, which for neutrons are assumed to be the delta function. The Fourier transform of the delta function is unity, which leaves the scattering amplitude independent of the momentum transfer,  $Q$ . This is an advantage compared to X-rays, as it gives diffractograms with well-defined and strong diffraction peaks at high  $Q$ .

The interaction between a neutron and an isotope's nucleus is described by the scattering length, which is defined as the amplitude of the spherically scattered neutron wave divided by the amplitude of the incoming neutron plane wave. The scattering length varies between neighboring atoms in the periodic table and between isotopes of the same

atoms. This is a great advantage when investigating neighboring elements or heavy and light atoms at the same time. Because of the complexity of the strong nuclear force, it is not possible to predict or calculate the scattering length for different isotopes, thus they have to be determined experimentally [14, 15].

## 2.6 Rietveld refinement

The Rietveld method is an analysis technique used in characterization of crystalline materials, where the diffraction pattern of a known structure is calculated and compared to a measured diffraction pattern. The method uses a least square approach to refine the theoretically calculated structure model until it resembles the collected data.

The diffraction pattern from the known structure is calculated from

$$Y_i^{calc} = S_F \sum_{j=1}^{nphases} \frac{f_j}{V_j^2} \sum_h^{npeaks} m_h L_h |F_{h,j}|^2 S_j (2\theta_i - 2\theta_{h,j}) P_{h,j} A_j + b h g_i. \quad (2.18)$$

The first factor is the scale factor,  $S_F \sum_{j=1}^{nphases} \frac{f_j}{V_j^2}$ , which adjusts the relative contribution of individual phases to the overall diffraction pattern. It is also used to calculate the weight fraction of the different crystalline phases in the material.

$L_h$  is called the Lorentz-Polarization factor. Diffraction occurs when reciprocal lattice-nodes cross the Ewald sphere, and if a node is in a diffracting position for a longer time, it will affect the intensity of the corresponding reflection. The time required for different reciprocal lattice nodes to cross the Ewald sphere will vary, depending on the method used to measure the intensity and the position of the nodes, and the Lorentz correction accounts for this effect. The polarization factor corrects for the loss in measured intensity due to the polarization state of the incoming beam.

The calculated structure factor,  $|F_{h,j}|$ , is given in 2.16 It includes the temperature dependent Debye Waller factor,  $B_n$ , which describes the thermal vibrations and isotropic displacement of the atoms. Due to symmetry in the structure, equivalent reciprocal lattice points will have the same intensities at the same Bragg angle. It is therefore unnecessary to calculate the intensities for corresponding Bragg peaks, as the intensity

## 2.6. RIETVELD REFINEMENT

---

can be calculated once and multiplied with the multiplicity factor  $m_{\underline{h}}$  of the  $\underline{h}$ 'th reflection. Due to how the material absorbs the radiation, X-ray radiation incident on a sample can be scattered both at the surface and throughout the sample. X-rays propagating in matter will be attenuated, and the absorption factor,  $A_j$ , accounts for the loss of intensity as function of the difference in pathways throughout the sample. The parameter  $P_{\underline{h},j}$  modifies the intensity due to preferred orientation.

$S_j(2\theta_i - 2\theta_{\underline{h},j})$  describes the shape of the profile, i.e. how the measured Bragg scattering is distributed around the ideal scattering angle, given by Bragg's law. It includes how the peak width, peak shape and asymmetry varies with scattering angle. Bragg peaks usually have a partly Gaussian and partly Lorentzian shape, and are thus well described by a pseudo-Voigt function, which is a linear combination of a Gaussian and Lorentzian shape.

The last part of equation 2.18 describes the background, and is defined as

$$bkg(2\theta_i) = \sum_{n=0}^{N_b} a_n (2\theta_i)^n \quad (2.19)$$

A quality of the fit of the calculated intensities to the measured intensities can be quantified by the relation

$$R_{w,p} = \sqrt{\frac{\sum_{i=1}^N \left[ w_i (Y_i^{exp} - Y_i^{calc}) \right]^2}{\sum_{i=1}^N w_i [Y_i^{exp}]^2}}. \quad (2.20)$$

By comparing this number to an expected R-factor, calculated from statistics of what a perfect model should look like,

$$R_{exp} = \sqrt{\frac{(N - P)}{\sum_{i=1}^N w_i [Y_i^{exp}]^2}}, \quad (2.21)$$

gives  $\chi^2$

$$\chi^2 = \frac{R_{w,p}}{R_{exp}} = \sqrt{\frac{\sum_{i=1}^N \left[ w_i (Y_i^{exp} - Y_i^{calc}) \right]^2}{(N - P)}}, \quad (2.22)$$

$\chi^2$  is then a measure of the quality of the calculated intensities, and should approach unity if the structure model is correct and there are no systematic errors in the fit [8, 13, 14, 16].

## 2.7 Infrared Spectroscopy

Infrared spectroscopy is a commonly used characterization method, where the interaction between infrared radiation and matter is used to identify and study chemicals. During the measurements, infrared radiation is passed through a sample, where fragments of radiation will be absorbed at particular energies corresponding to frequencies of the vibrational parts of molecule. Molecules can thereby be identified by comparing the absorption peaks to a data bank of spectra, and the method is useful for both sample identification and structure analysis.

Different atoms possess different electronegativity, which can lead to polar molecules. The dipole moment is defined by the magnitude of the charge difference and the distance between the centers of the charges. A molecular bond is IR-active if its electric dipole moment change during the vibration. A vibrating polar molecule will have a fluctuating dipole moment, which causes an electric field. This field will interact with the electric field from the incoming infrared radiation. If the frequency of the incoming radiation is proportional to the natural vibrations of the molecule,  $\bar{\nu}$ , it will lead to absorption.

The absorption of infrared radiation can lead to both rotational and vibrational transitions depending on the energy of the incoming radiation. The vibrational motions can be observed as stretching modes, where the bond lengths are altered, and bending modes, where the angle between the bonds are altered. The different types of bending and stretching is shown in figure 2.10 . A molecule consisting of  $N$  atoms will have a total of  $3N$  degrees of freedom. In a linear molecule ( $3N - 5$ ) of the degrees of freedom are fundamental vibrations, whereas in a non-linear molecule ( $3N - 6$ ) are fundamental vibrations [17].

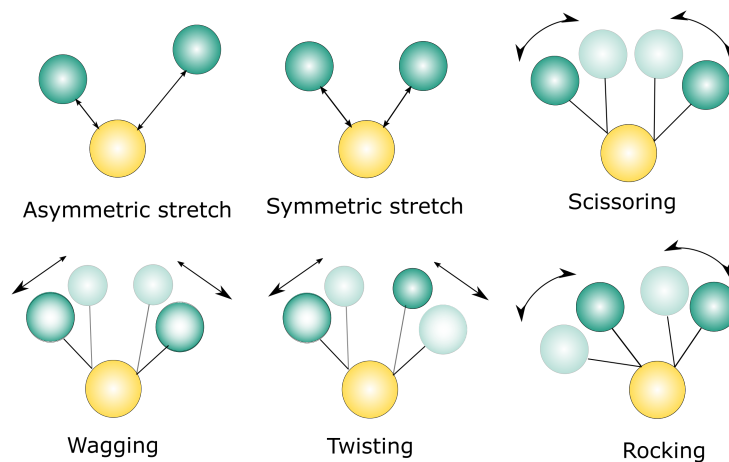


Figure 2.10: The figure illustrates different vibrational modes of a non-linear molecule.

## 2.8 Symmetry and vibrational modes

A symmetry operation transforms an object into a new orientation which is equivalent to the old one. Molecules can be classified in groups according to their symmetry properties, which can be used to predict or explain some of the molecule's properties, such as possible vibrational modes. The five spatial symmetry operations that constitute the symmetry groups are given in table 2.2, with their corresponding transformational matrixes. Each point group  $G$  has a set of transformational matrixes  $R$  representing all symmetry operations within that point group. Irreducible representations of these matrixes are presented in character tables, summarizing all symmetry operations within the point group. An example of a character table is shown in table 2.3. The point group is indicated in the top left-hand corner of the table, and all of the symmetry operations inherent to the group are listed to the right. The subsequent rows list all of the possible symmetry species. They describe a set of irreducible transformations for the particular symmetry operation applies, where  $+1$  and  $-1$  indicates whether the symmetry operation is symmetric or antisymmetric. The basis functions on the right hand side of the

Symmetry operation	Symbol	Transformation Matrix
Identity	E	$\begin{bmatrix} 1 & 0 & 0 \\ 0 & 1 & 0 \\ 0 & 0 & 1 \end{bmatrix}$
Reflection	$\sigma$	$\begin{bmatrix} -1 & 0 & 0 \\ 0 & -1 & 0 \\ 0 & 0 & -1 \end{bmatrix}$
Rotation	$C_n$	$\begin{bmatrix} \cos(\frac{2\pi}{n}) & \sin(\frac{2\pi}{n}) & 0 \\ -\sin(\frac{2\pi}{n}) & \cos(\frac{2\pi}{n}) & 0 \\ 0 & 0 & 1 \end{bmatrix}$
Improper rotation	$S_n$	$\begin{bmatrix} \cos(\frac{2\pi}{n}) & \sin(\frac{2\pi}{n}) & 0 \\ -\sin(\frac{2\pi}{n}) & \cos(\frac{2\pi}{n}) & 0 \\ 0 & 0 & -1 \end{bmatrix}$
Inversion	i	$\begin{bmatrix} -1 & 0 & 0 \\ 0 & -1 & 0 \\ 0 & 0 & -1 \end{bmatrix}$

Table 2.2: Symmetry operations and transformation matrixes.

table gives the symmetry of mathematical functions, and can be used to find the symmetry of atomic orbitals and linear movement along the x-, y-, and z-axis.

$C_{2v}$	$E$	$C_2$	$\sigma_v$	$\sigma'_v$			IR/Raman active
$A_1$	+1	+1	+1	+1	$z$	$x^2, y^2, z^2$	IR, Raman
$A_2$	+1	+1	-1	-1		$xy$	Raman
$B_1$	+1	-1	+1	-1	$x$	$xz$	IR, Raman
$B_2$	+1	-1	-1	+1	$y$	$yz$	IR, Raman

Table 2.3: Character Table for the  $C_{2v}$  Group. A indicates symmetrical rotation around principal axis, while B indicates asymmetrical rotation around the principal axis. The two last columns give the basis functions, indicating whether the modes are IR and/or Raman active.

Group theory, and the mathematical functions, can be used to predict the expected number of infrared and Raman active modes in a molecule. A vibrational mode is infrared active if it has the same symmetry as a component of the electric dipole vector (x, y, z). Molecular vibrations are Raman active if the polarizability tensor for the molecule changes.

## 2.8. SYMMETRY AND VIBRATIONAL MODES

---

The polarizability tensor transforms as second order functions of  $x$ ,  $y$ , and  $z$  [18, 19].



# Chapter 3

---

## Experimental methods

### 3.1 Sample preparation

As the materials are sensitive to air, all sample handling was done under purified argon atmosphere ( $<1$  ppm  $O_2$  and  $H_2O$ ) in an MBraun Unilab glove box. Powder of  $LiBH_4$  ( $\geq 95\%$ ) and  $LiBr$  ( $\geq 99,0\%$ ), both from Sigma-Aldrich, were used as starting materials to make  $2LiBH_4 + LiBr$ , LB. The different amount of the powders were weighed out using a Mettler toledo AG204 DeltaRange balance, before they were mixed in a mortar with a pestle. The mixture was transferred to a stainless steel container, containing 50 10mm-balls of stainless steel, and sealed, before it was placed in the ball mill, "Fritsch GmbH Planetary Micro MillPulverisette 7", outside the glovebox. The mill rotates the container at high speed around two axes at the same time, forcing the materials to react inside the container. In order to get the desired results, it is important to regulate the milling parameters, such as rotational speed, milling time, atmosphere inside the container, ball-to-powder ratio and temperature.

A batch of in total 5 grams of the LB material was mixed in the planetary mill at 500 rotations per minute, where the milling time was set to two minutes followed by a two-minute break, which was repeated 60 times. The resultant powder was heat treated at 423 K for 14 hours under a 20 bar hydrogen atmosphere.

## 3.2. POWDER X-RAY DIFFRACTION

---

W% LB	W% LPS	M%LB	M% LPS	LB <sub>x</sub> LPS <sub>(1-x)</sub>
25	75	29	71	x = 0.25
33	67	38	62	x = 0.33
50	50	55	45	x = 0.50
67	33	72	28	x = 0.67
75	25	79	21	x = 0.75

Table 3.1: Mass percentage and molar percentage of the prepared samples.

The  $3\text{Li}_2\text{S} + \text{P}_2\text{S}_5$  material, LPS, was made from  $\text{Li}_2\text{S}$  (Sigma-Aldrich, 99.98%) and  $\text{P}_2\text{S}_5$  (Sigma-Aldrich, 98%), and mixed by the same procedures as mentioned above. The batch of in total 5 grams was milled for 20 hours without break, at 370 rotations per minute.

The two materials were further mixed in the different weight ratios that are shown in table 3.1. The milling time was set to 5 hours, with 30 minutes rest between each hour, at 370 rpm. The powders were heat treated at 423 K for 14 hours under 20 bar hydrogen atmosphere.

## 3.2 Powder X-ray diffraction

The samples were measured on the Bruker AXS D8 Advanced diffractometer at IFE, and the results were mainly used for phase identification. The samples were later measured at the Swiss-Norwegian Beam Line BM01 at the European Synchrotron Radiation Facility in Grenoble, France, and these results were used for more thorough Rietveld refinements.

### 3.2.1 X-ray diffraction, home lab

A powder X-ray diffractometer consists mainly of a X-ray source, a sample holder and a detector. On the diffractometer at IFE, the source and the detector are attached by two arms to a goniometer, which is a construction designed to measure the angle between the incident and reflected beam. The arms can rotate around the goniometer axis, where the sample is placed. The setup is illustrated in figure 3.1. The X-ray tube of the diffractometer has a copper anode which supplies X-rays with

wavelength  $\lambda_{Cu-K\alpha} = 1,54060 \text{ \AA}$ , and the detector of the instrument is a Lynx-Eye silicon strip detector.

The samples for PXD were grinded in a mortar before they were packed with a 3 mm glass stick into 5 mm glass capillaries. To make sure that the sample fill the X-ray beam the capillaries must be filled with approximately two cm of powder. The capillary is then cut and glued before it is moved out of the glovebox and to the diffractometer. The sample is attached to the goniometer and adjusted until it is parallel to the goniometer axis.

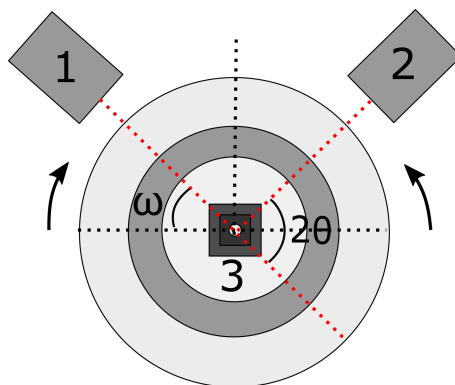


Figure 3.1: This figure illustrates the setup of the Bruker AXS D8 Advanced diffractometer, where (1) is the source, (2) is the detector, and (3) is the sample holder. The source and detector can rotate around the goniometer axis, which is where the sample is placed.

### 3.2.2 Synchrotron radiation

A synchrotron is a particular type of particle accelerator, and is used to generate extremely brilliant radiation in the X-ray range. Electrons are accelerated up to velocities approaching the speed of light by strong magnetic fields inside a circular shaped tube, illustrated in figure 3.2. The radiation is generated when the electrons are forced to change directions. This is either done by bending magnets which keep the electrons in the circular track, or by insertion devices that make the electron beam oscillate. The high relativistic energy results in a beam that can be considered as nearly parallel to the velocity trajectory of the electron, and

### 3.3. POWDER NEUTRON DIFFRACTION

---

can be used to achieve high resolution measurements.

The samples were measured in 5 mm capillaries, using a 2D-detector, Pilatus 2M.

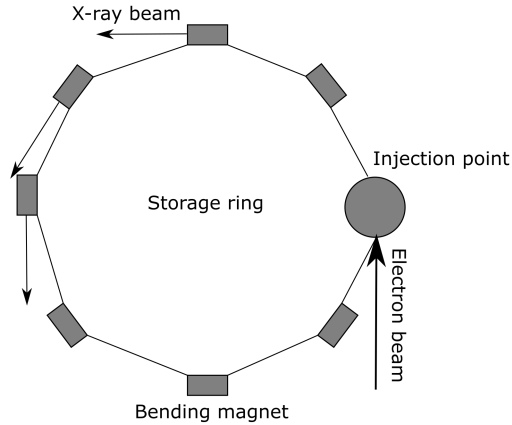


Figure 3.2: Illustration of the synchrotron storage ring.

## 3.3 Powder neutron diffraction

When neutrons are used for diffraction experiments they have to be produced in nuclear reactions, either in reactor cores or in spallation reactions. An illustration of a typical powder neutron diffractometer at a reactor source is shown in figure 3.3. The produced neutrons are passed through a moderator, where the speed of the fast neutrons are reduced by letting them collide repeatedly with light atoms in the moderator. The average energies of the emerging neutrons are proportional to the temperature in the moderator, and the relation between the momentum of the neutrons and their wavelength can be found using the de Broglie relation. The range of the wavelength is therefore decided in the moderator. Before the neutron beam is passed through the sample and detected, it is monochromated by a single-crystal monochromator [8].

The powder neutron diffraction (PND) data were collected with the high-resolution powder neutron diffractometer PUS at the JEEP II reactor at IFE. A cylindrical vanadium sample holder was used, filled with approximately 1 cm<sup>3</sup> of powder. Monochromatic neutrons with wave-

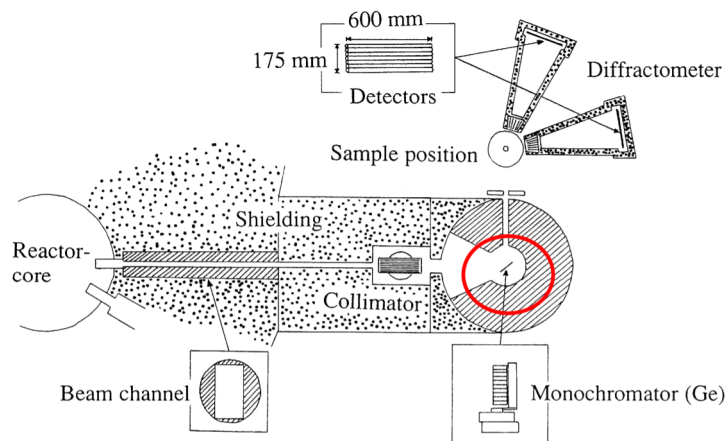


Figure 3.3: Illustration of the PND instrumentation, and the propagation path of the neutrons.

length  $1.555\text{\AA}$  were obtained from a Ge(511) focusing monochromator. The detector unit consists of two banks of seven position-sensitive  $^3\text{He}$  detectors, each covering  $20^\circ$  in  $2\theta$ . Intensity data were collected from  $2\theta=10\text{--}130^\circ$  in steps of  $\Delta(2\theta) = 0.05^\circ$ .

### 3.4 Electrochemical Impedance Spectroscopy

The impedance spectroscopy is performed on a symmetrical cell, connected by two wires to a BioLogic SP-300 Potentiostat. The cell is exposed to a frequency dependent potential perturbation and the current response is measured.

Approximately 200 mg of the annealed powders were introduced in a 10 mm die set, and pressed uniaxial at around 370MPa for 15 minutes, using a "PIKE Technologies Crushit"-press. The pressed pellets were weighed and their thicknesses were measured, before they were sandwiched between two lithium foils. Further, the pellets were placed inside a cell, which is described in figure 3.4. To improve the connection at the lithium-electrolyte interface, the cells were annealed at 333 K for 4 hours.

### 3.5. CYCLIC VOLTAMMETRY

---

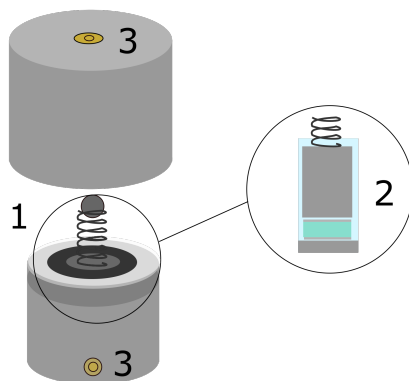


Figure 3.4: Illustrates the cell used for impedance measurements. The pellet is placed as shown in (2), and the spring in (1) ensures good contact between the pellet and the lithium as the cell is sealed. (3) indicates where the wires of the potentiostat are connected.

The instrument was programmed to start the measurement when the open circuit voltage (OCV) reached a stabilization limit of 0.1 mV/h. During the impedance measurements, potential waves with the amplitude of 2mV were impressed on the system in a frequency range of 1 MHz - 1 Hz. The measurements were performed in heating and cooling runs from room temperature to 328 K, with 10 K step intervals, and the measurements were repeated for three times at each temperature.

## 3.5 Cyclic voltammetry

Cyclic voltammetry is a technique used to study the electrochemical properties of a material by investigating the reduction and oxidation processes of the chemical species. It is performed by applying a potential scan to the working electrode, and measuring the current response. The scan rate is held constant, but the scan is performed in both forward and reversed directions.

The potential of the working electrode is measured against a reference electrode, which is held at a fixed potential. The applied potential at the working electrode is swept at a constant sweep rate, given in V/s. The excitation signal is illustrated in the left graph of figure 3.5. From  $t_0$  to

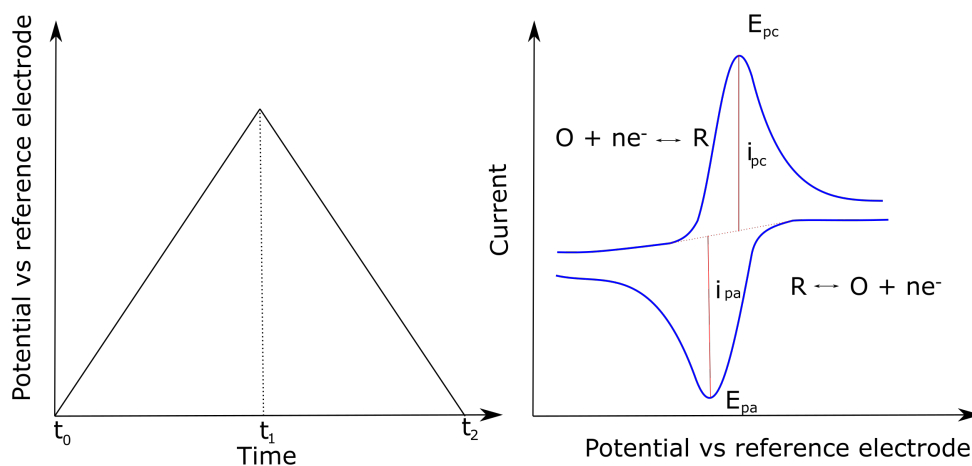


Figure 3.5: The left part of the figure illustrates the applied potential at the working electrode during the forward and backwards scans. The right part illustrates the current as function of applied potential, during oxidation and reduction of the species.

$t_1$ , a reducing potential is applied to the cell. If there are reducible chemical species in the system, the cathodic current will increase during this time step. When the concentration of the reducible species is depleted, the reduction potential ( $E_{pc}$ ) of the species is reached, and the cathodic current will decrease. From  $t_1$  to  $t_2$ , the scan rate is reversed, and the reduced chemical species will start to oxidize if the redox couple is reversible. The total process is illustrated in the right part of figure 3.5. The more reversible the reactions are, the more similar will the shape of the curves during oxidation and reduction be [20, 21].

Pellets of 100 mg were pressed uniaxially in a 10 mm die set at 370MPa for 5 minutes. The pellets were further sandwiched between lithium foils and gold foils, where the gold functioned as the working electrode and lithium as both reference and oxidation electrode. The pellets were then inserted into the same type of cell as used for impedance measurements, and the resultant asymmetric cell was placed inside a Termax heat cabinet set at 298 K. The experiments were conducted using a Biologic SP-300 potentiostat, with a sweep rate of 1mV/s in the voltage range from -0.5 to 5 V.

### 3.6. CELL ASSEMBLY

---

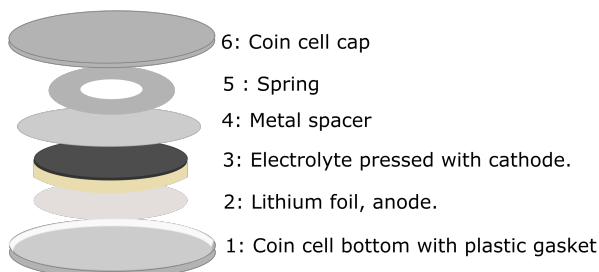


Figure 3.6: Illustration of the cell components in a coin cell, and in which order they are stacked inside the cell.

## 3.6 Cell assembly

Titanium disulfide,  $\text{TiS}_2$ , mixed in a 2:3 weight ratio with the solid electrolyte and lithium metal were used as cathode and anode materials. A pellet of approximately 80 mg solid electrolyte was prepressed uniaxially in a 10 mm die set at around 200 MPa for 5 minutes. Approximately 10 mg of the cathode material was evenly distributed at the surface of the pellet, before the electrode and electrolyte were pressed together at 370 MPa for 15 minutes. The lithium foil was brushed on both sides to remove any surface contamination or films, cut to a 10 mm circular shape, and placed on to the electrolyte. The pellets were further assembled to coin cells, as shown in figure 3.6. To ensure good contact when the cell is sealed, a plastic gasket was placed inside the coin cell bottom. Further, the pellet was put inside the cell bottom, with the lithium side pointing downwards. A metal spacer was placed over the pellet, and a metal spring on top of this again. The purpose of the spacer and the spring is to fill the internal space of the cell, and to provide good contact between the electrodes and the electrolyte. The cell cap was then placed on top of the spring, before the cell case was hermetically sealed by a crimping machine. The resultant battery was annealed at 343 K for 5 hours to ensure good contact between the pellet and the lithium foil.

The two most promising electrolyte materials,  $\text{LB}_{0.33}\text{LPS}_{0.67}$  and  $\text{LB}_{0.50}\text{LPS}_{0.50}$ , were chosen for battery test, and two cells of each composition were assembled. The cycling of the batteries was performed at 323 K, using a Termax heat cabinet and an Arbin cyler. The cells were set



to be stabilized at the open circuit voltage (OCV) for 24 hours, before the cycling could start. In the first cycle, the cells were discharged and charged at a cycling rate of C/100 from 2.7 V vs. Li+/Li to 1.6 V vs. Li+/Li. For the next cycles, the cells were programmed to be cycled at a cycling rate of C/20 in the same potential range.

### 3.7 Infrared Spectroscopy

Fourier transform infrared spectroscopy is a technique used to obtain the infrared spectrum of absorption or emission of a sample. This is done by shining light of different wavelengths on the sample, and measure how well the sample absorbs at the given wavelengths.

The special feature with an FTIR spectrometer compared to dispersive spectrometers, is that rather than shining a monochromatic beam of light at the sample, the interferometer produces a signal comprising a continuum over the IR frequency range. Thus, the signal can be measured quickly, and the measuring time per sample is reduced to a few seconds.

The source generates radiation, which is passed through the sample located in the interferometer, before it is conducted into the detector. The signal from the detector is amplified and converted into a digital signal, before being transferred to a computer where the Fourier transform calculations are executed, and the user obtains the frequency spectrum of the sample.

All samples were measured at the ALPHA II FTIR Spectrometer at IFE.

### 3.8 Differential Scanning Calorimetry

Differential scanning calorimetry, DSC, and thermogravimetric analysis, TGA, are thermoanalytical techniques used to investigate thermophysical properties of materials while they are exposed to temperature changes. In DSC, the amount of heat required to increase the temperature of a sample and a reference is measured, and can be used to investigate the thermal energy released or consumed as the sample undergoes physical or chemical changes. In TGA, the mass of the sample is measured. The information collected from DSC and TGA can be supplementary, and

### 3.8. DIFFERENTIAL SCANNING CALORIMETRY

---

the thermoanalytical experiments in this thesis were both performed simultaneously with a Netzsch STA 449 F3 Jupiter apparatus.

A crucible containing the sample material and an empty reference crucible are placed on a thermally conducting surface, which is connected to a high precision weight that enables TGA to be performed in-situ. Two thermocouples are placed underneath the respective crucibles, and the temperature difference between the sample and the reference can therefore be monitored. An oven is placed above the surface with the samples, and it can be lowered and thereby enclose the crucibles as they are heated. The oven is connected to a gas circuit, so that the atmosphere and gas flow inside the enclosed space can be regulated by the gas. Because the surface that holds the crucibles is made out of a thermally conducting material, any difference registered during the heating of the sample and the reference must be ascribed to the sample [22].

A heating-program with an empty crucible must be run before the measurements can be performed. The result from this run is called the baseline for the measurement, which accounts for the background contribution to the heat flux signal generated by the empty crucible. A baseline program with linear heating at rate  $5 \frac{K}{min}$  up to  $400 \text{ }^\circ\text{C}$  was measured, and the same reference crucible and baseline was used when measuring all the samples. Approximately 6-10 mg of the powders was used during each measurement.

# Chapter 4

---

## Results

The aim of the work can be divided into two, where one part is to investigate the conductivity and structure of the samples, and the second part is to study whether the materials have the required properties to be used as electrolytes in actual batteries.

In the first part of this chapter, the measured impedance from EIS will be presented, followed by structural analyses based on the techniques of powder X-ray diffraction (PXD), powder neutron diffraction (PND) and infrared spectroscopy (IR). The second part will provide results concerning the materials properties due to battery requirements, obtained from thermal analyses (DSC), cyclic voltammetry (CV) and battery cycling. Figure 4.1 gives an overview of which methods that have been performed on which samples.

Sample	EIS	PXD	PND	IR	DSC	CV	Cycling
LB <sub>0.25</sub> LPS <sub>0.75</sub>	x	x	-	x	x	-	-
LB <sub>0.33</sub> LPS <sub>0.67</sub>	x	x	x	x	x	x	x
LB <sub>0.50</sub> LPS <sub>0.50</sub>	x	x	-	x	x	x	x
LB <sub>0.67</sub> LPS <sub>0.33</sub>	x	x	-	x	x	-	-
LB <sub>0.75</sub> LPS <sub>0.25</sub>	x	x	-	x	x	-	-

Table 4.1: Overview of which methods that have been performed on which samples.

## 4.1 Impedance measurements

The room temperature impedances for all samples are presented by Nyquist plots in figure 4.1. The figure shows that the samples have a semicircular shape at high frequencies, which is characteristic for ionic conductivity, and a straight line in the low frequency area, characteristic for ion blocking electrodes.

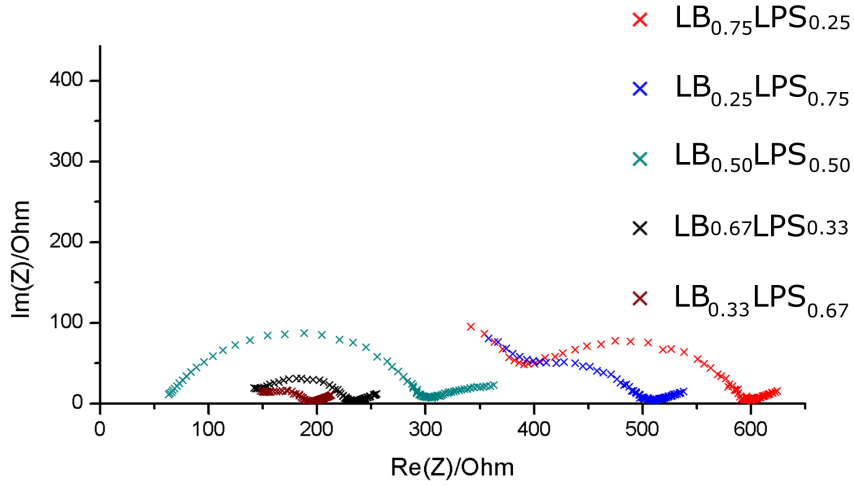


Figure 4.1: Nyquist plots of all the samples, measured at 21 °C.

The total resistances of the materials are found at the intersection between the real axis and the continued semicircle, and are used when calculating the ionic conductivities, which is given as

$$\sigma = \frac{d}{R_{tot}A}, \quad (4.1)$$

where  $d$  is the thickness of the pellet,  $A$  the area of the contact surface between the pellet and the electrode. The calculated conductivities as function of temperature are presented in figure 4.2, which shows that the conductivities can be divided into three groups. The first group consists of  $LB_{0.33}LPS_{0.67}$  and  $LB_{0.67}LPS_{0.33}$ , which exhibit high and similar

ionic conductivities.  $\text{LB}_{0.50}\text{LPS}_{0.50}$  obtains comparable values at elevated temperatures, but the conductivity at room temperature differs from  $\text{LB}_{0.33}\text{LPS}_{0.67}$  and  $\text{LB}_{0.67}\text{LPS}_{0.33}$ , and it is therefore preferable to study the sample separately. Lastly,  $\text{LB}_{0.25}\text{LPS}_{0.75}$  and  $\text{LB}_{0.75}\text{LPS}_{0.25}$  exhibit similar and low ionic conductivities, and compose the last group. The conductivity values at room temperature and at 55 °C are extracted from the figure, and given in table 4.2 together with the calculated activation energies.

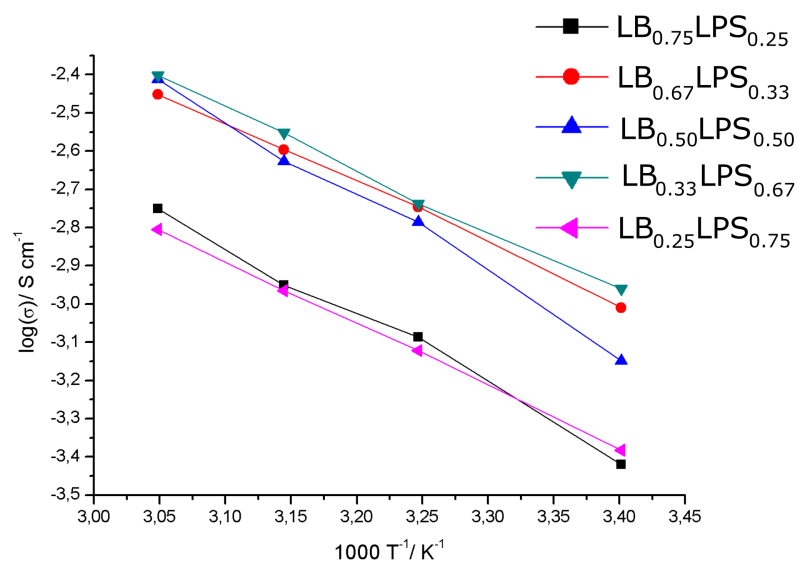


Figure 4.2: Presentation of the conductivity for the different samples as function of temperature

#### 4.1. IMPEDANCE MEASUREMENTS

---

Sample	Activation energy [eV]	Conductivity 21 °C [S/cm]	Conductivity 55 °C [S/cm]
LB <sub>0.25</sub> LPS <sub>0.75</sub>	0.39(5)	$4.1(2) \cdot 10^{-4}$	$1.5(8) \cdot 10^{-3}$
LB <sub>0.33</sub> LPS <sub>0.67</sub>	0.33(1)	$1.1(7) \cdot 10^{-3}$	$4.0(2) \cdot 10^{-3}$
LB <sub>0.50</sub> LPS <sub>0.50</sub>	0.43(8)	$7.1(5) \cdot 10^{-4}$	$3.9(2) \cdot 10^{-3}$
LB <sub>0.67</sub> LPS <sub>0.33</sub>	0.34(3)	$9.8(6) \cdot 10^{-4}$	$3.5(2) \cdot 10^{-3}$
LB <sub>0.75</sub> LPS <sub>0.25</sub>	0.35(1)	$3.5(2) \cdot 10^{-4}$	$1.8(7) \cdot 10^{-3}$

Table 4.2: The calculates activation energies for the different samples, and their conductivities at room temperature and at 55 °C.

#### Interpreting the shape of the curves

The semicircular shape in the Nyquist plots can be represented by a RC-circuit in an equivalent circuit representation, and the capacitance values for the representation give the domain of which the feature is attributed to. The capacitance values are extracted and given in table 4.3, and state that the measured impedances for all the samples lie in the grain boundary range. Thus the resistances  $R_{circle}$  in the same table describe the grain boundary resistance of the samples. The table show that LB<sub>0.50</sub>LPS<sub>0.50</sub> has the greatest grain boundary resistance, followed by LB<sub>0.75</sub>LPS<sub>0.25</sub> and LB<sub>0.25</sub>LPS<sub>0.75</sub>, while the two samples showing highest conductivity values, LB<sub>0.33</sub>LPS<sub>0.67</sub> and LB<sub>0.67</sub>LPS<sub>0.33</sub>, have the lowest grain boundary resistance. The LB<sub>0.50</sub>LPS<sub>0.50</sub> sample behaves differently than the other, in the way that it has the highest grain boundary resistance, while the total resistance lie in the mid-range. Figure 4.2 shows that also the temperature dependence of the conductivity of LB<sub>0.50</sub>LPS<sub>0.50</sub> is different from the others, as it goes to being one of the best ionic conductors at 55 °C, and it has the highest activation energy.

Sample	$R_{tot}$ [ $\Omega$ ]	$R_{circle}$ [ $\Omega$ ]	C [F]
x = 0.25	506(15)	183(5)	$8(1) \cdot 10^{-9}$
x = 0.33	196(6)	37(1)	$6.8(2) \cdot 10^{-8}$
x = 0.50	380(9)	237(8)	$5.3(7) \cdot 10^{-8}$
x = 0.67	217(7)	78(2)	$4.1(3) \cdot 10^{-8}$
x = 0.75	560(17)	221(7)	$4.5(6) \cdot 10^{-8}$

Table 4.3: The measured resistances and the calculated capacitance from the impedance plots at room temperature. All capacitance values are in the grain boundary range.

It is observed that most of the samples deviate from the semicircular shape at the high frequency area, and that the semicircles are depressed. The features do not impact the total resistance, nor the conductivity calculations, and are therefore not further investigated.

### Temperature stability

An important criterion for an electrolyte material is that the same physical properties are obtained at the same temperature after heating and cooling. The impedance of the samples were measured in heating and cooling runs, and the results are given in figures A.1 - A.5 in appendix. The figures show the measured impedances before and after heating varies the most in  $LB_{0.25}LPS_{0.75}$  and  $LB_{0.75}LPS_{0.25}$ , and the least in  $LB_{0.50}LPS_{0.50}$  and  $LB_{0.33}LPS_{0.67}$ . Variations in measurements before and after heating can be an indication of poor connection at the electrode electrolyte interface. This may therefore imply that  $LB_{0.50}LPS_{0.50}$  and  $LB_{0.33}LPS_{0.67}$  form advantageous connections to the electrode material.

A difference in measured impedance before and after heating have also been observed in other reports [3, 6], and the authors have use the values measured during cooling in their discussion. Thus, the measured data obtained during cooling are used in this thesis.

### Uncertainty

It is common to study the results obtained from impedance measurements by an equivalent circuit approximation to separate and quantify different contributions. The method has not been used in this work, and the total resistance has been extracted from the intersection between the

#### 4.1. IMPEDANCE MEASUREMENTS

---

real axis and the continued semicircle, which introduce a higher degree of uncertainty in the results, as illustrated in figure 4.3.

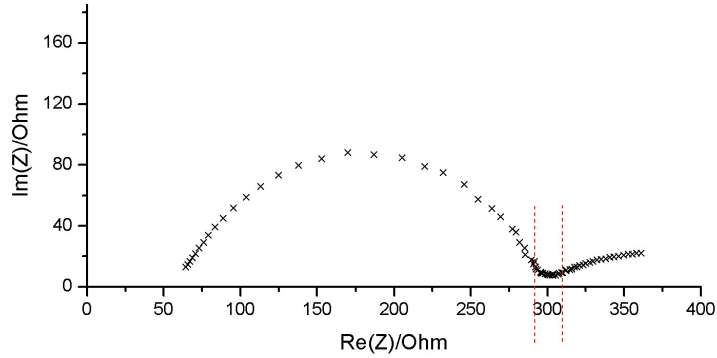


Figure 4.3: The total resistance is found at the intersection between the continued semicircle and the real axis. The extracted value is determined by how the continued semicircle is drawn, which introduces an uncertainty,  $\Delta\Omega$ .

The total uncertainty of the impedance measurements can be divided into two. The first group contains the parameters in equation 4.1, namely the thickness and the radius of the pellet, and the extracted value of the total resistance. By investigating the uncertainty of each parameter and the parameters propagation of error, one can estimate how they affect the results. This is done in appendix A.1, and it shows that the relative uncertainty from these parameters is around 6%. The second group is composed of parameters that are known to affect the result, but would require a much more thorough inquisition to investigate their contributions to the total uncertainty. Some examples are the temperature and the density of the materials. Therefore, it is inaccurate to give the conductivity as a specific number after preparing only one cell from one batch of material, but the impedance measurements give a good indication of the range of the values. <sup>1</sup>

---

<sup>1</sup>The instrument has an internal uncertainty of around 0,5 %, which is negligible compared to the calculated uncertainty.



## 4.2 Structural analysis

### 4.2.1 Powder X-ray diffraction

The  $\text{Li}(\text{BH}_4)_{0.67}\text{Br}_{0.33}$  phase was studied in the pre-work of this thesis, where several interesting features were identified. As the features also are observed in the mixed materials, the  $\text{Li}(\text{BH}_4)_{0.67}\text{Br}_{0.33}$  will be briefly discussed in the first part of this section, before the crystal structure of the mixed materials will be presented.

#### $\text{Li}(\text{BH}_4)_{0.67}\text{Br}_{0.33}$

The goal of milling and annealing  $2\text{LiBH}_4 + \text{LiBr}$  was to obtain a solid solution of the hexagonal phase of  $\text{Li}(\text{BH}_4)_{0.67}\text{Br}_{0.33}$  at room temperature, which was confirmed through Rietveld refinements in TOPAS

The  $\text{LiBH}_4$  structure consist originally of light atoms. Bromide has a relatively high atomic number, and it will tend to dominate the X-ray scattering from the structure as it is introduced into the structure. In order to investigate how the amount of bromide influences the diffraction pattern, TOPAS was used to simulate diffraction patterns of  $\text{LiBH}_4$  as function of increased bromide content, and the results are shown in figure 4.4. It is easy to see that the relative intensity changes drastically already for 10 % bromide substitution compared to pure hexagonal  $\text{LiBH}_4$ , and the relative intensities change further up to 20 % bromide substitution. However, at higher substitution levels, the relative intensities are more or less unchanged. This means that the bromide anions completely dominate the scattering already at 20% substitution. Refinements of higher substitution levels are therefore uncertain because the bromide occupancy will correlate strongly with the scale factor in the Rietveld refinements.

## 4.2. STRUCTURAL ANALYSIS

---

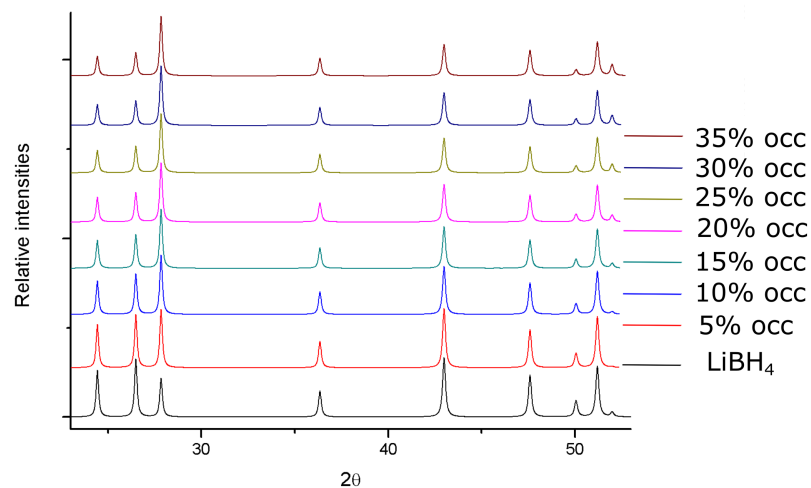


Figure 4.4: Simulated diffraction patterns of LiBH<sub>4</sub> with an increasing amount of bromide substitution

During the first refinements, it was assumed that bromide was substituted into the same position as borohydride in the crystal structure. The refined diffraction pattern suffered from a systematic error in relative intensity. This error disappeared by letting the  $z$  position of the borohydride and bromide be refined independently. To investigate how the displacement affects the crystal structure, the structural data was used to plot the unit cell of hexagonal LiBH<sub>4</sub>, and compare it to the original structure, figure 4.5. The figure shows that the displacement results in altered distances between the lithium ions and borohydride and bromide ions.

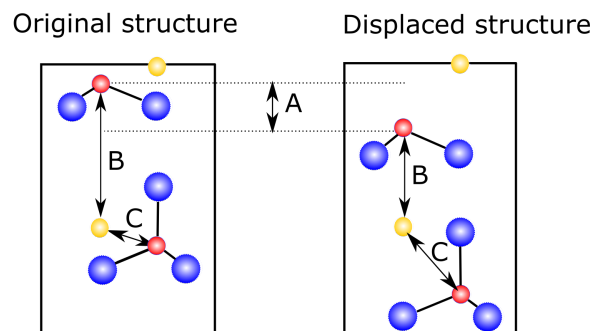


Figure 4.5: Unit cell of  $\text{LiBH}_4$ , where the anion displacement in  $z$ -direction is illustrated. The unit cell to the left shows the original structure. To the right, the  $\text{BH}_4^-$  anion is moved to the position found from the refinements of the LB sample, marked with A in the figure. B and C shows that the distances between  $\text{Li}^+$  and  $\text{BH}_4^-$  are altered as a result of the substitution and displacement.

### Refinements of the mixed samples

The EVA software was used for phase identification by matching the observed Bragg peaks to phases containing Li, B, H and/or Br in the PDF-4 database, and the HT- $\text{LiBH}_4$  and  $\text{Li}_6\text{PS}_5\text{Br}$  were identified in the samples. The crystal structures of the samples were further investigated by Rietveld refinements in TOPAS. The refined weight fractions of the crystalline phases in the samples are given in table 4.4. The table shows that the LB-phase is first observed in the  $\text{LB}_{50}\text{LPS}_{50}$  sample, and that  $\text{LB}_{0.25}\text{LPS}_{0.75}$  and  $\text{LB}_{0.33}\text{LPS}_{0.67}$  only contain  $\text{Li}_6\text{PS}_5\text{Br}$  in their crystal structure. The starting materials of the samples contained a considerable amount of both boron and hydrogen, and these atoms have to be present in the sample in some form.

## 4.2. STRUCTURAL ANALYSIS

	Li <sub>6</sub> PS <sub>5</sub> Br, w%	HT-Li(BH <sub>4</sub> ) <sub>y</sub> Br <sub>(1-y)</sub> , w%
LB <sub>0.25</sub> LPS <sub>0.75</sub>	100	-
LB <sub>0.33</sub> LPS <sub>0.67</sub>	100	-
LB <sub>0.50</sub> LPS <sub>0.50</sub>	80.33(2)	19.67(2)
LB <sub>0.67</sub> LPS <sub>0.33</sub>	51.84(1)	48.16(1)
LB <sub>0.75</sub> LPS <sub>0.25</sub>	37.83(9)	62.17(1)

Table 4.4: Weight percentage of the different phases in the crystalline part, extracted from TOPAS.

Li<sub>6</sub>PS<sub>5</sub>Br belongs to a group of materials called argyrodites, and it is a halide substituted version of Li<sub>7</sub>PS<sub>6</sub>, space group F $\bar{4}3$ m. The substituted bromide ions can be distributed over two crystallographic positions, 4a and 4d. These atomic positions are illustrated in an excerpt of the unit cell shown in figure 4.6.

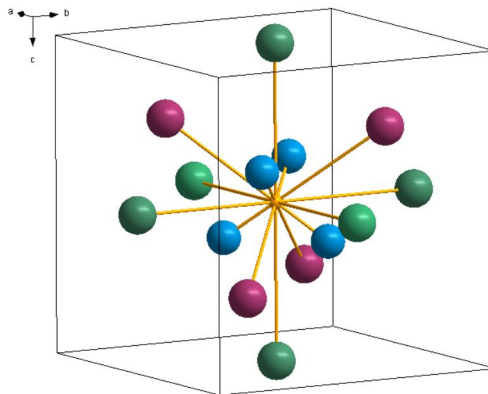


Figure 4.6: An excerpt of the unit cell, where the possible positions for bromide are highlighted. Yellow and blue represents phosphorus at the 4b site and sulfur at the 16e respectively. Green represents the 4a sites and pink the 4d sites, where sulfur can be substituted by bromide.

From the pre-work of the LB sample, it was suggested that the starting materials had fully reacted, as there were no signs of excess LiBr in the diffractogram. Thus, no free bromide will be available for substitution into the argyrodite structure, and the substituted bromide has to appear from LB. Table 4.5 gives the amount of bromide substituted

$\text{LB}_x\text{LPS}_{(1-x)}$	Occ 4a	Occ 4d	Unit cell volume [ $\text{\AA}^3$ ]
$\text{LB}_{0.25}\text{LPS}_{0.75}$	0.333(7)	0.28(9)	997.2(7)
$\text{LB}_{0.33}\text{LPS}_{0.67}$	0.33(6)	0.225(6)	1001.5(2)
$\text{LB}_{0.50}\text{LPS}_{0.50}$	0.23(1)	0.12(1)	1001.7(2)
$\text{LB}_{0.67}\text{LPS}_{0.33}$	0.23(1)	0.12(1)	1000.5(1)
$\text{LB}_{0.75}\text{LPS}_{0.25}$	0.19(1)	0.07(2)	1002.6(2)

Table 4.5: Refined occupancy of bromide in  $\text{Li}_6\text{PS}_4\text{Br}$  at the 4a and 4d sites for the samples. The table also show the refined unit cell volumes.

$\text{LB}_x\text{LPS}_{(1-x)}$	Z-pos $_{\text{BH}_4}$	Z-pos $_{\text{Br}}$	Bromide occupancy	Volume [ $\text{\AA}^3$ ]	Temperature factor [ $\text{\AA}^2$ ]
$\text{LB}_{0.50}\text{LPS}_{0.50}$	0.742(4)	0.606(4)	0.57(7)	102.87(2)	3.2(1)
$\text{LB}_{0.67}\text{LPS}_{0.33}$	0.691(2)	0.582(4)	0.44(2)	102.81(1)	4.47(8)
$\text{LB}_{0.75}\text{LPS}_{0.25}$	0.696(1)	0.583(4)	0.45(1)	103.11(1)	5.38(7)
Reference	0.553(1)	0.553(1)		110.04	8.6(4)

Table 4.6: Bromide occupancies, temperature factors and atomic position for the  $\text{Li}(\text{BH}_4)_y\text{Br}_{(1-y)}$  phase in the different samples.

into  $\text{Li}_6\text{PS}_5\text{Br}$ . The table shows that the highest occupancies are found in the samples where no crystalline  $\text{LiBH}_4$  is present,  $\text{LB}_{0.25}\text{LPS}_{0.75}$  and  $\text{LB}_{0.33}\text{LPS}_{0.67}$ , and that the occupancies decrease as function of LB content in the starting materials.

The refined bromide occupancies of the LB-phase in the mixed materials in table 4.6 shows that the bromide occupancies are refined to values above 20 % for all samples, which imply that they are uncertain due to previous discussions. However, the substitution can be estimated from the refined unit cell volumes. As the ionic radius of the bromide is smaller than the ionic radius of borohydride, the unit cell volume will decrease as function of bromide content. The refined unit cell volumes in table 4.6 are similar for all samples, which imply that the bromide occupations should be similar as well. In other words, it is assumed that the amount of bromide in the LB phase is the same for all samples, while it decreases as the amount of available bromide increases for the  $\text{Li}_6\text{PS}_5\text{Br}$  phase, which is a contradiction.

The refined z-positions of bromide and borohydride in the LB phase is

## 4.2. STRUCTURAL ANALYSIS

---

given in table 4.6. By comparison to the reference, it is obvious that the displacement is most evident in  $\text{LB}_{0.50}\text{LPS}_{0.50}$ , while the displacements in  $\text{LB}_{0.67}\text{LPS}_{0.33}$  and  $\text{LB}_{0.75}\text{LPS}_{0.25}$  varies in the third decimal.

The refined temperature factors of the  $\text{Li}_6\text{PS}_5\text{Br}$  phase are given in table 4.7. The table shows that the temperature factors differ at both different sites and samples, and that they are higher than what is expected for solids. High temperature factors indicate that there is structural disorder in the samples. As sulfur and bromide have different charge and atomic radius, the structural environments around the sites will be altered when sulfur ions at specific sites are substituted by bromide ions. The refinements describe the average conditions at the sites, while the local conditions will vary at the different sites, and this structural disorder can be observed as high temperature factors.

	Temp. fac 4a [ $\text{\AA}^2$ ]	Temp. fac 4d [ $\text{\AA}^2$ ]	Temp. fac 4b [ $\text{\AA}^2$ ]	Temp. fac 16e [ $\text{\AA}^2$ ]
$\text{LB}_{0.25}\text{LPS}_{0.75}$	3.514	1.937	1.388	2.830
$\text{LB}_{0.33}\text{LPS}_{0.67}$	4.254	2.584	2.143	4.288
$\text{LB}_{0.50}\text{LPS}_{0.50}$	2.670	2.894	3.349	4.215
$\text{LB}_{0.67}\text{LPS}_{0.33}$	2.932	2.291	2.942	4.102
$\text{LB}_{0.75}\text{LPS}_{0.25}$	1.638	3.092	4.946	4.392

Table 4.7: Refined temperature factors at the different sites in  $\text{Li}_6\text{PS}_5\text{Br}$  for the samples.

### Diffractograms

The presence of amorphous content leads to diffuse scattering, thus the background of the diffractograms can be used as a first indication to predict whether the samples contain amorphous phases. The diffractograms are presented in figure 4.7 - 4.11, and figure 4.7 show that the background of  $\text{LB}_{0.25}\text{LPS}_{0.75}$  is particularly uneven. This is also the sample containing most of the amorphous LPS in its starting material. The refined structure model of this sample and the  $\text{LB}_{0.33}\text{LPS}_{0.67}$  sample were similar, implying that the structure of the materials are similar. However, the starting materials are quite different, thus it is suggested that the crystal structure of the materials are similar, while  $\text{LB}_{0.25}\text{LPS}_{0.75}$  contain a considerable amount of amorphous phases in addition. From the back-

grounds in figure 4.9 and 4.11 it can be discussed whether  $\text{LB}_{0.50}\text{LPS}_{0.50}$  and  $\text{LB}_{0.75}\text{LPS}_{0.25}$  also contain amorphous phases.

The diffractograms show that the calculated intensities do not match the measured intensities perfectly. Small additional peaks are observed, which imply that an unidentified crystalline phase is present. The peaks are especially visible in  $\text{LB}_{0.50}\text{LPS}_{0.50}$ . If an additional phase is present, the program will try to compensate for its intensity, which can be one of the reasons for the mismatch in calculated and measured intensities at some peaks. Other reasons can be anisotropic disorder, false minima and/or substitutions at other sites, but this is out of the scope for this thesis to investigate.

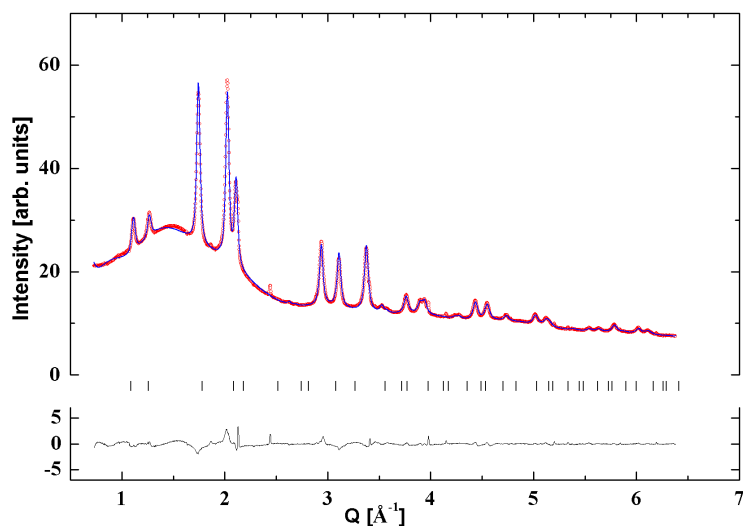


Figure 4.7: Rietveld fit to the SR-PXD data of the annealed sample of  $\text{LB}_{0.25}\text{LPS}_{0.75}$

## 4.2. STRUCTURAL ANALYSIS

---

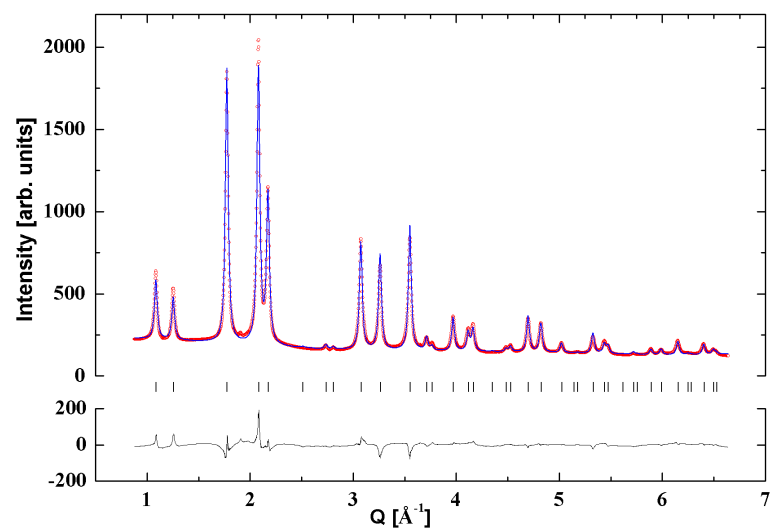


Figure 4.8: Rietveld fit to the SR-PXD data of the annealed sample of  $\text{LB}_{0.33}\text{LPS}_{0.67}$

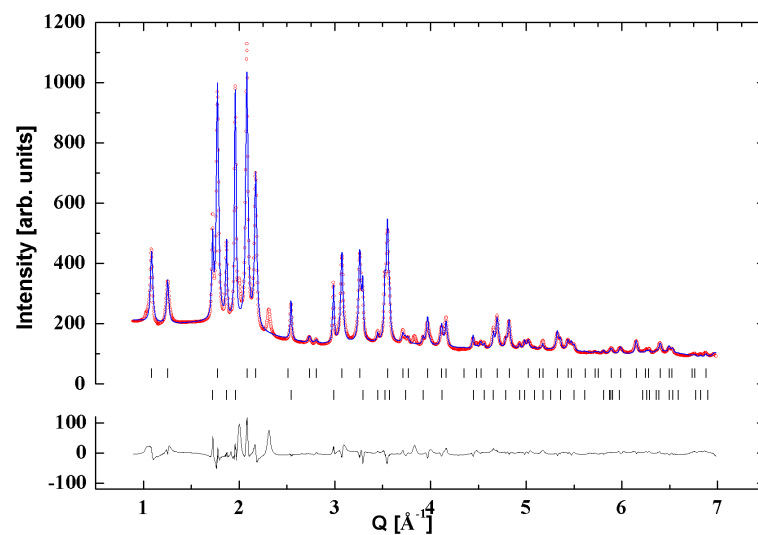


Figure 4.9: Rietveld fit to the SR-PXD data of the annealed sample of  $\text{LB}_{0.50}\text{LPS}_{0.50}$



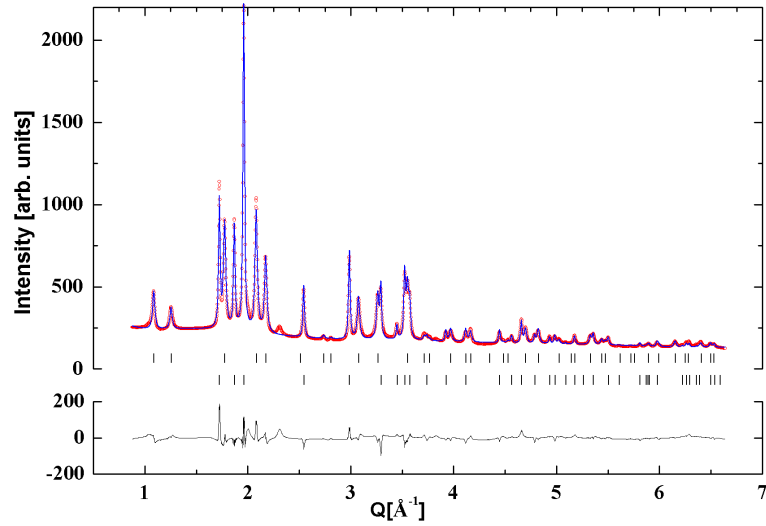


Figure 4.10: Rietveld fit to the SR-PXD data of the annealed sample of  $\text{LB}_{0.67}\text{LPS}_{0.33}$

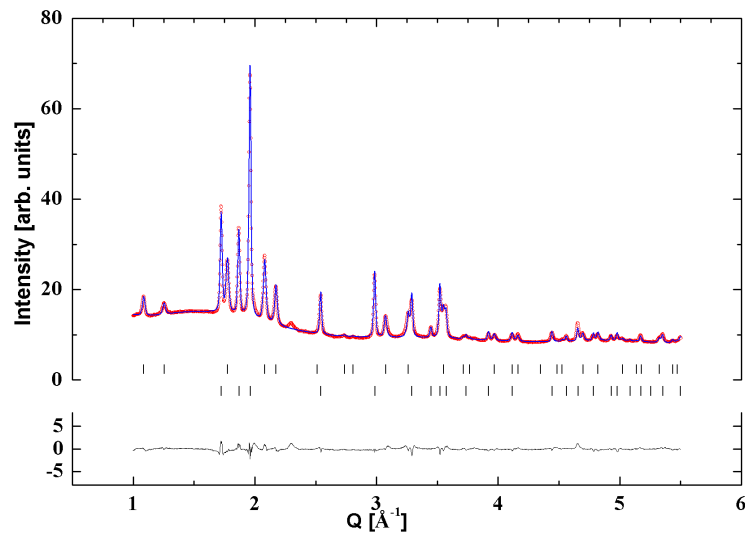


Figure 4.11: Rietveld fit to the SR-PXD data of the annealed sample of  $\text{LB}_{0.75}\text{LPS}_{0.25}$

### 4.2.2 Infrared spectroscopy

The LPS material is amorphous and it has therefore not been possible to characterize its content or structure from X-ray diffraction. However, infrared spectroscopy assigns energy to bonds in the structure, and can also be used for materials with no long range order. The technique was therefore used both to study the LPS material, as well as investigate whether the  $\text{BH}_4^-$  anion is still visible in the samples where it had disappeared from the crystal structure.

The starting materials are used as references for the mixed materials, and will therefore be presented first. Figure 4.12 shows the spectrum obtained from all samples.

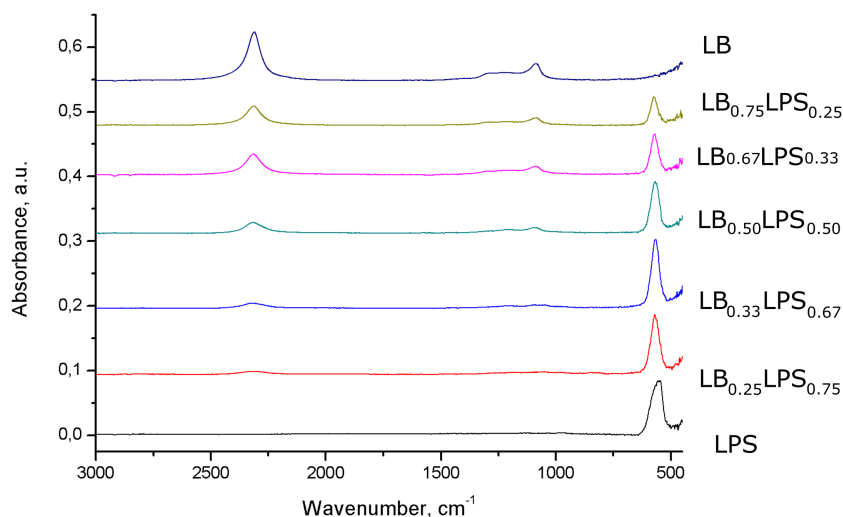


Figure 4.12: Infrared spectra of all the samples.

#### LB

A more thorough comparison between the infrared spectra obtained from  $\text{LiBH}_4$  and LB is given in appendix B.1.2. Figure B.2 in appendix shows that the main peaks due to stretching,  $2000\text{-}2500\text{ cm}^{-1}$ , and bending,  $1000\text{ - }1500\text{ cm}^{-1}$ , are still present in the spectrum, but the intensities are decreased, as well as the number of modes. The increased number

of modes can be explained by a change in symmetry when going from orthorhombic to hexagonal phase, leading to a reduction in degeneracy of modes, and smeared out peaks. The decrease in peak intensity can be explained by the altered surroundings around the  $\text{BH}_4^-$  anions. As the  $\text{BH}_4^-$  anion is substituted by a bromide at some of the sites, the structure goes from being well defined to less defined, where both neighboring atoms and distances between the ions have changed.

## LPS

The spectrum measured from amorphous LPS shows that it has one peak at around  $550 \text{ cm}^{-1}$ . This peak is both broad and asymmetric, indicating that it may consist of several overlapping peaks. Phosphorus and sulfur can exist in different varieties. The vibrational modes of some different varieties have been assigned from a mixture of  $y\text{Na}_2\text{S} + (1-y)\text{P}_2\text{S}_5$  [23], and are given in table 4.8. By comparing the table and the peak found from the LPS-spectra, it is suggested that the LPS material contains both  $[\text{P}_2\text{S}_6]^{2-}$ ,  $[\text{P}_2\text{S}_6]^{4-}$  and  $[\text{PS}_4]^{3-}$ . The modes of  $[\text{PS}_4]^{3-}$  and  $[\text{P}_2\text{S}_6]^{2-}$  lie close in wavenumber, and a possible splitting of peaks at the given wavenumber can be observed in figure 4.12. The peaks are slightly shifted to the left, which can be attributed to an increase of the length of the molecular chains [24].

Ion	Wavenumber [ $\text{cm}^{-1}$ ]
$\text{P}_2\text{S}_6^{4-}$	583
$\text{P}_2\text{S}_6^{2-}$	549
$\text{PS}_4^{3-}$	543

Table 4.8: Different PS-ions with related infrared wavenumber, found from of  $y\text{Na}_2\text{S} + (1-y)\text{P}_2\text{S}_5$  [25].

## The mixed samples

The spectra obtained from the mixed samples show that all of the samples have peaks in the stretching and bending regions of  $\text{BH}_4^-$  and a peak attributed to P-S-bonds. It also shows that the intensity of the peaks attributed to  $\text{BH}_4^-$  increase as function of LB content, and vice versa for the PS-peaks. The figure shows that the PS-peaks in the mixed materials are more symmetric compared to the peak in the LPS-sample. This can

## 4.2. STRUCTURAL ANALYSIS

---

indicate that there has been a reaction, leading to a reduced number of different species in the samples. To better compare the different samples, the center of the peaks have been extracted and are shown in table 4.9. The table shows that the center of the PS-peaks are slightly shifted towards higher wavenumbers for the mixed samples, which be attributed to an increase in the long range order of the material. Also, the peak attributed to  $\text{BH}_4^-$  is slightly shifted in some of the samples, which can be explained by the altered environment around the  $\text{BH}_4^-$  anion.

Sample	Wavenumber $_{BH_4}$ [ $\text{cm}^{-1}$ ]	Wavenumber $_{PS}$ [ $\text{cm}^{-1}$ ]
LPS	-	556
$\text{LB}_{0.75}\text{LPS}_{0.25}$	2311	570
$\text{LB}_{0.67}\text{LPS}_{0.33}$	2321	568
$\text{LB}_{0.50}\text{LPS}_{0.50}$	2316	571
$\text{LB}_{0.33}\text{LPS}_{0.67}$	2312	571
$\text{LB}_{0.25}\text{LPS}_{0.75}$	2311	576
LB	2311	-

Table 4.9: Shows the center of the peaks of the infrared spectra obtained from all samples. It shows that some of the peaks are shifted compared to the starting materials.

A ratio between the presence of the different anions in the mixed samples can be obtained by comparing the area of the peak intensities attributed to the anions. The ratio between the presence of  $\text{BH}_4^-$  and  $\text{PS}_4^{3-}$  found from infrared spectroscopy for the samples are plotted in figure 4.13, as function of the same ratio calculated in the starting materials. The infrared spectra gives information about the presence of  $\text{BH}_4^-$  and  $\text{PS}_4^{3-}$  anions, but not the state of their presence. The figure shows an approximately linear behavior, indicating that the relation between the anions in the starting material and measured from IR are relatively similar. The intensity of the peaks are associated with vibrations of functional groups in the molecules, and different functional groups give different intensities in the spectrum. The slope of the curve is attributed to the relative intensity difference between the molecular vibrations of the two species.

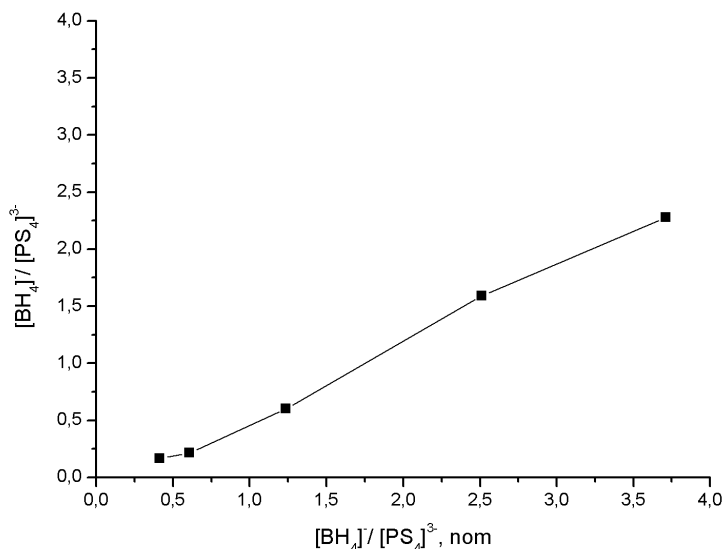


Figure 4.13: Ratio between  $\text{BH}_4^-$  and  $\text{PS}_4^{3-}$  in mixed materials found from infrared spectroscopy, as function of the same relation in the starting materials.

### 4.2.3 Powder neutron diffraction

From X-ray diffraction it was concluded that no crystalline  $\text{BH}_4$  is present in  $\text{LB}_{0.25}\text{LPS}_{0.75}$  and  $\text{LB}_{0.33}\text{LPS}_{0.67}$ . However, the presence of  $\text{BH}_4^-$  in the same samples are confirmed by infrared spectroscopy. Neutron and X-ray diffraction are sensitive to different atomic properties, and the same change in crystal structure can affect the diffraction pattern quite differently. Both  $^{11}\text{B}$  and  $\text{D}$  have large neutron scattering cross sections, and it was therefore beneficial to study the  $\text{LB}_{0.33}\text{LPS}_{0.67}$  sample by neutron diffraction to examine whether any new information could be provided.

During the first Rietveld refinement in TOPAS, the same structure model as used for X-ray diffraction was used, with the correct isotopes inserted. The refined bromide occupancies are given in table 4.10, together with the values obtained from X-ray diffraction. Structural information from neutron and X-ray diffraction are complimentary, and the occupancies should be refined to similar values for the two techniques. However, the occupancies are refined to completely different values. To investigate

## 4.2. STRUCTURAL ANALYSIS

---

	Occ 4a	Occ 4d
Neutron diffraction	0.51(7)	0.88(6)
X-ray diffraction	0.33(6)	0.22(5)

Table 4.10: Refined bromide occupation in  $\text{Li}_6\text{PS}_5\text{Br}$  of a  $\text{LB}_{0.33}\text{LPS}_{0.67}$  sample from both x-ray and neutron diffraction.

how the amount of substituted bromide influences the diffraction pattern, the refined occupancies from PXD were inserted into the structure model for the deuterated sample and vice versa. The calculated and measured diffraction patterns for the samples are shown in figures B.6 and B.7 in appendix , and it is obvious from the figures that the structure model obtained from X-ray diffraction does not fit the data from neutron diffraction.

Both bromide, sulfur and borohydride have similar atomic radii (1.96, 1.84 and 2.05 Å for  $\text{Br}^-$ ,  $\text{S}^{2-}$ ,  $\text{BH}_4^-$  respectively), which is one of the premises for chemical substitution. It may therefore be possible that the  $\text{BH}_4^-$  anion has been substituted into the argyrodite structure.

To test the hypothesis, a new structure model for the argyrodite phase was constructed, with borohydride, bromide and sulfur inserted at the 4a and 4d sites. It is not possible to refine the occupations of the different ions at the different sites freely, thus the occupations were first estimated. The neutron scattering cross sections given in table 4.11 show that the  $\text{BD}_4^-$  anion consist of five strong scatterers. By adding their contributions, it is obvious that this anion is the strongest neutron scatterer of the three possible substitutional ions, thus it should be easy to localize for the refinement program. The occupations of the  $\text{BD}_4^-$  and sulfur anion were therefore refined freely, and it was assumed that the refined  $\text{BD}_4^-$ -occupations were close to their actual values. The remaining occupancies at the sites were divided between sulfur and bromide, by calculations based on their scattering lengths.

The occupancy of borohydride were held fixed while the occupancies for boron and sulfur were refined simultaneously, which gave a new structure model that fit both diffractograms. The diffractograms with new structure model are shown in figures 4.14 and 4.15, and the refined occupancies are given in table 4.12. The figures suggest that it is possible for both bromide and borohydride to be substituted into the  $\text{Li}_7\text{PS}_6$ -phase.

Isotope	Coh XS [b]
2H	5.592
7Li	0.619
11B	5.56
P	3.307
S	1.0186
Br	5.8

Table 4.11: The coherent scattering cross section of the different isotopes in the measured material

	$S_{4a}$	$Br_{4a}$	$BH_{44a}$	$S_{4d}$	$Br_{4d}$	$BH_{44d}$
Occupation	0.377	0.433	0.190	0.410	0.370	0.220

Table 4.12: The refined occupancies for the possible substitutional ions at sites 4a and 4d, obtained from combined refinements of diffraction patterns from both x-ray and neutron diffraction.

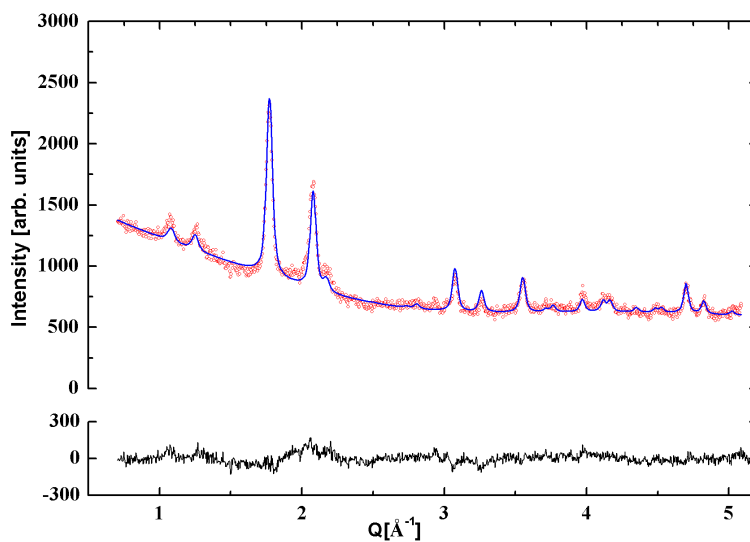


Figure 4.14: Structure model obtained from combined refinements fitted with PND data.

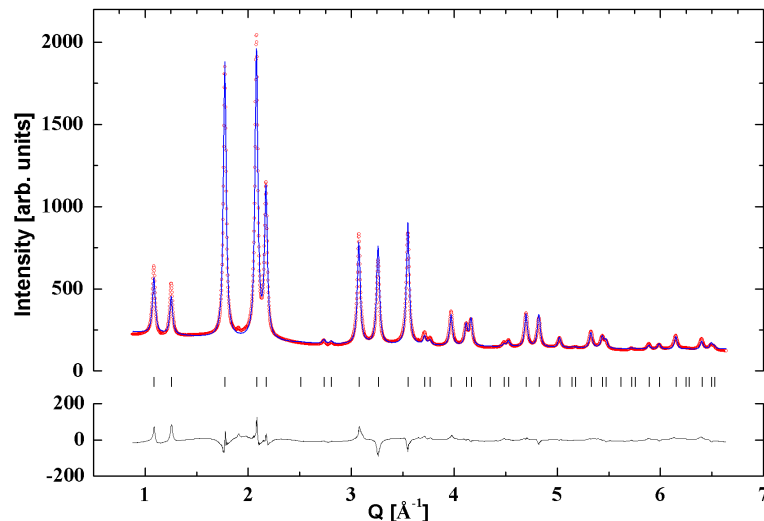


Figure 4.15: Structure model obtained from combined refinements fitted with SR-PXD data.

### 4.3 Analysis of $LB_xLPS_{1-x}$ as electrolyte material

This section will provide results from techniques concerning battery properties and performance.  $LB_{0.33}LPS_{0.67}$  and  $LB_{0.50}LPS_{0.50}$  were regarded as the most promising electrolyte materials, as they showed the highest conductivity values at 55 °C and the most stable impedance values before and after heating. Due to restricted capacity and time, the two samples were selected for further investigation.

#### 4.3.1 Thermal stability

The DSC-measurements obtained from all of the samples are given in figure 4.16. The DSC-curve of the LB sample shows that an endothermic event occur at around 350 °C, which is attributed to the melting of the material. The melting temperature of hexagonal  $LiBH_4$  is 275 °C, and the results show that it is increased for the LB. No endothermic peak is observed in the mixed materials, indicating that the melting temperatures are increased to above the range of the measurement temperatures.



For the LPS phase, a sharp exothermic peak is observed at approximately 230 °C, which is attributed to the crystallization of the material.

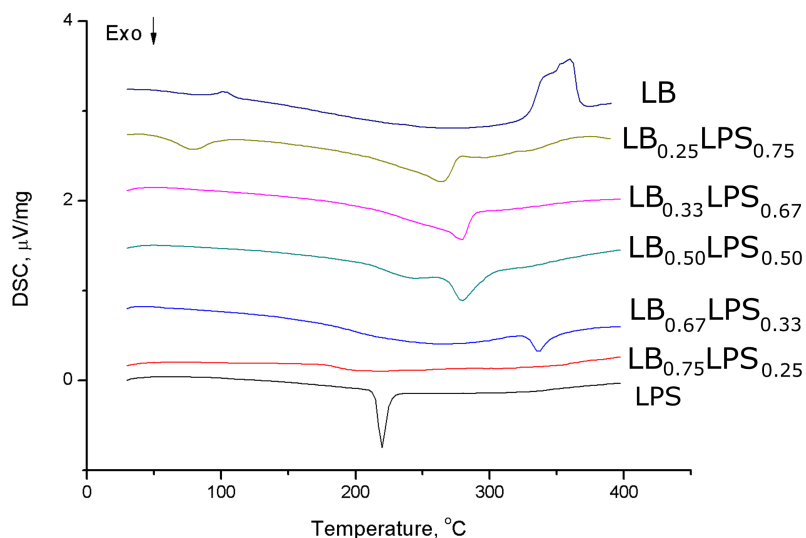


Figure 4.16: DSC curves for all of the samples

The figure shows that an exothermic event is observed for the mixed samples at around 250 °C to 350 °C, and the event is associated with a weight loss. It appears at lowest temperature for the LB-rich sample, and the temperature of the event is increasing as the LB-content is decreasing, where it has completely disappeared for the sample containing the least LB. To investigate whether the event is connected to a recrystallization of the samples, the  $\text{LB}_{0.75}\text{LPS}_{0.25}$  was heat treated up to 300 °C and measured with X-ray diffraction. The diffraction pattern is given in figure C.1 in appendix. It clearly shows that the sample is recrystallized, as no trace of the earlier identified phases are visible. Using the Eva software, LiBr and  $\text{Li}_2\text{S}$  were identified, but several more peaks remain unidentified.<sup>2</sup>

Batteries are normally used in temperatures below 100 °C - 150 °C, thus it is important that the electrolyte material is stable in this temper-

<sup>2</sup>It is out of the scope of this thesis to identify the crystal structure, as its onset temperature is above the temperature range for batteries.

### 4.3. ANALYSIS OF $LB_xLPS_{1-x}$ AS ELECTROLYTE MATERIAL

ature range. The figure shows that the samples are thermally stable up to at least 250 °C, except the  $LB_{0.75}LPS_{0.25}$  where an exothermic event is observed at around 80 °C. The conductivity values of this sample are too low for it to be used in batteries, thus it is out of scope for the thesis to further investigate the event.

#### 4.3.2 Electrochemical stability

The cyclic voltammograms of  $LB_{0.33}LPS_{0.67}$  and  $LB_{0.50}LPS_{0.50}$  after initial cycles are shown in figure 4.17 and 4.18. Cyclic voltammetry is here used to investigate electrolyte reactions at high voltages, and thereby study the electrochemical stability of the materials. As the lithium electrode is set to be the reference and oxidation electrode, and gold as the working electrode, the figures show the process deposition of lithium at the working electrode for increased voltages, and the reversed process for decreasing voltages. The reversible lithium dissolution and stripping is observed at around 0 V, and no irreversible oxidation current appears up to 5 volt. This implies that the electrolytes are electrochemically stable up to 5 V, suggesting that both electrolytes have wide potential windows.

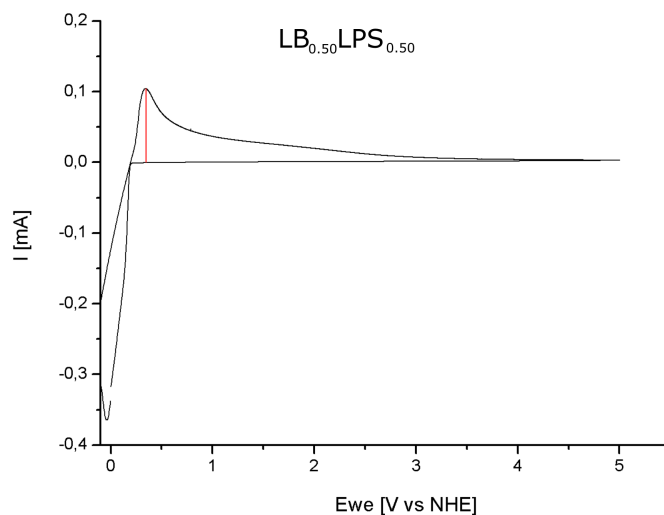


Figure 4.17: Cyclic voltammogram of  $LB_{0.50}LPS_{0.50}$ , one complete cycle.

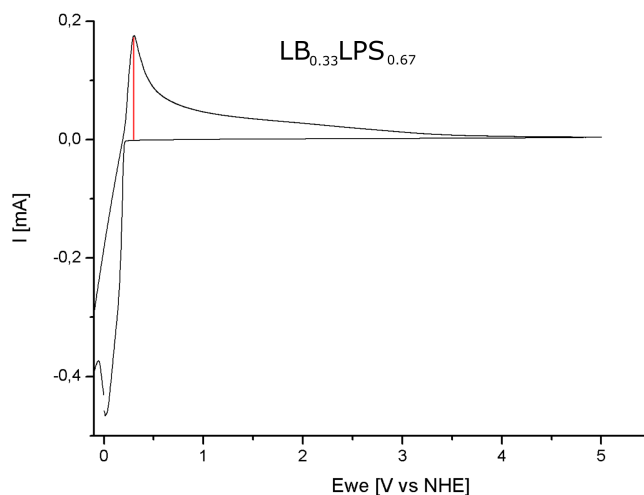


Figure 4.18: Cyclic voltammogram of LB<sub>0.33</sub>LPS<sub>0.67</sub>, one complete cycle.

The anionic peak current for the two samples are marked in the figures. The value of the anionic peak current in LB<sub>0.33</sub>LPS<sub>0.67</sub> is larger than in LB<sub>0.50</sub>LPS<sub>0.50</sub>. This observation suggests that the internal resistance in the LB<sub>0.50</sub>LPS<sub>0.50</sub> is greater than in LB<sub>0.33</sub>LPS<sub>0.67</sub>, which is in consistency with both impedance and cycling measurements.

Cyclic voltammetry can also be used to investigate the reversibility of the redox reactions in the electrolyte, namely if all of the initial analyte can be recovered after a forward and reverse scan cycle. One of the criteria is that the ratio between the cathodic peak current ( $I_{pc}$ ) and the anodic peak current ( $I_{pa}$ ) should be close to one. Figures 4.17 and 4.18 show that this criterion is not fulfilled. The measured current is related to the surface of the electrodes, and the species of interest might be absorbed on the electrode surface. If some of the deposited lithium is stuck on the surface of the gold electrode, it will affect the system conditions. The lithium ion is small, and it is therefore probable that it can be adsorbed on the subsurface of gold.

### 4.3.3 Battery test

Three of the discharge/charge cycles obtained from the  $LB_{0.33}LPS_{0.67}$  sample are presented in figure 4.19, and information about the cycling performance is extracted and presented in table 4.13.

The figure shows one complete charge/discharge cycle with cycling rate  $\frac{C}{100}$ , and two cycles with cycling rate  $\frac{C}{20}$ . The anode material,  $TiS_2$ , has a theoretical capacity of 239 mAh/g, and the figure shows that an utilization ratio of 92 % of the theoretical value is achieved after the first cycle, and 85 % after the third cycle. The capacity is slightly decreased when going from cycling rate  $\frac{C}{100}$  to  $\frac{C}{20}$ , which is expected owing to the increase of polarization on the surface of the electrode.

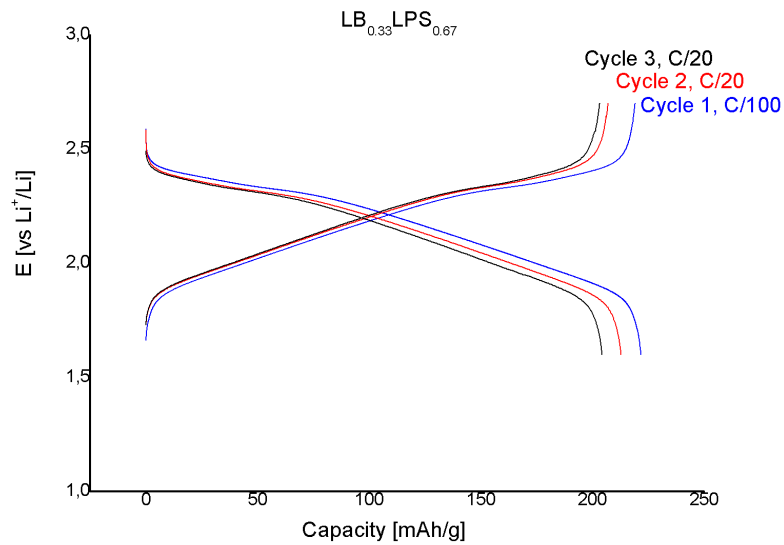


Figure 4.19: Battery cycles of  $LB_{0.33}LPS_{0.67}$  at two different cycling rates.

It was not possible to get a complete and satisfying cycle from the  $LB_{0.50}LPS_{0.50}$  sample.

Cycle number	Cycling rate [ $\frac{mA}{g}$ ]	Discharge capacity [ $\frac{mAh}{g}$ ]	Charge capacity [ $\frac{mAh}{g}$ ]	Coulombic efficiency
1	C/100	222	219	$\sim 99\%$
2	C/20	219	213	$\sim 99\%$
3	C/20	204	203	$\sim 99\%$

Table 4.13: Extracted values for discharge and charge capacities, and their coulombic efficiency for a battery with  $LB_{0.33}LPS_{0.67}$  as electrode material.

#### 4.3. ANALYSIS OF $LB_xLPS_{1-x}$ AS ELECTROLYTE MATERIAL

# Chapter 5

---

## Discussion

### 5.1 Conductivity and structure

The measured conductivities of the different samples varies, and the aim of the work has been to find a relation between sample content and measured conductivities. First, the conductivities were compared to the weight percentages of the crystalline phases in the samples. PXD of the samples in the high-conductivity group showed that their crystal content is quite different, where  $\text{LB}_{0.33}\text{LPS}_{0.67}$  contain only  $\text{Li}_6\text{PS}_5\text{Br}$  in it's crystal structure, while  $\text{LB}_{0.33}\text{LPS}_{0.67}$  contain approximately equal amounts of  $\text{Li}_6\text{PS}_5\text{Br}$  and LB. A similar relation is observed for the samples showing lowest conductivity values. The conductivity could therefore not be directly related to the phase content, thus the crystalline phases were investigated more thoroughly in each sample.

#### Observations investigated in $\text{Li}(\text{BH}_4)_{(1-y)}\text{Br}_y$

The high temperature phase of  $\text{LiBH}_4$  is known as a novel lithium ion conductor [2]. The relation between ionic conductivity and bromide content in  $\text{Li}(\text{BH}_4)_{(1-y)}\text{Br}_y$  has been investigated [26], and the maximum conductivity was measured in the sample with the lowest possible bromide occupation for the hexagonal phase, namely  $y = 0.29$ . The decrease in ionic conductivity for higher occupational values was explained by the decreasing unit cell volume, giving a less defined diffusion pathway for

## 5.1. CONDUCTIVITY AND STRUCTURE

---

lithium ions. As discussed in the results, it is difficult to quantify the bromide occupancy in the LB structure from X-ray diffraction, as the relatively heavy bromide will tend to dominate the X-ray scattering from the structure. However, as the refined unit cell volumes are approximately constant for all samples, the bromide occupations should also be similar, and therefore not influence the differences in measured conductivity.

During the refinements, the  $z$  position of the borohydride and bromide had to be refined independently in order to obtain satisfying results. It was found that the anions were displaced compared to the original structure. The displacement alters the distances between the lithium ions and the bromide and borohydride ions in the structure, and the feature was tried related to the conductivity. For one of the samples in the high-conductivity groups and one of the samples in the low-conductivity group, the  $z$ -positions of bromide and borohydride were refined to values varying in the third decimal, and the amount of the LB phase is significant in both samples. As their conductivities are quite different it seems unlikely that this feature alone have a great impact on the measured conductivities.

### Observations investigated in $\text{Li}_6\text{PS}_5\text{Br}$

The substitution of sulfide by a bromide in  $\text{Li}_6\text{PS}_5\text{Br}$  introduces lithium ion vacancies to maintain charge balance [27]. The bromide can be substituted at two crystalline positions in the structure, and the distribution of the substituted halides at the different sites thereby decides how local diffusivity transforms to macroscopic conductivity [28]. Based on this, one would assume that the sample with highest occupancy of bromide at both substitutional positions,  $\text{LB}_{0.25}\text{LPS}_{0.75}$ , induces more vacancies, and thereby exhibit highest conductivity. However, the sample belongs to the low conductivity group.<sup>1</sup> Both the high and the low conductivity group contain structures with the highest and the lowest bromide occupations, which imply that the occupations can not separately be related to the measured conductivities in this work.

The temperature factors indicate if there is structural disorder in the materials. To investigate whether structural disorder affects the conductivity, the temperature factors were also tried connected to the conductivity trend, but neither this comparison lead to an obvious correlation.

---

<sup>1</sup>The same sample show an uneven background in its diffraction pattern, and it was therefore suggested that it contains amorphous material. It may be that this influences the conductivity negatively.



### Introducing the new structure, $\text{Li}_{7-x-y}\text{PS}_{6-x-y}\text{Br}_x(\text{BH}_4)_y$

The  $\text{Li}_6\text{PS}_5\text{Br}$  phase was studied by powder neutron diffraction in an deuterated sample of  $\text{LB}_{0.33}\text{LPS}_{0.67}$ . Results obtained from PXD and PND did not match, and a new structure model was introduced, with the possibility of both bromide, borohydride and sulfur being present at the substitutional sites of the structure. The diffraction patterns obtained from PND and PXD were refined simultaneously, and the new structure model correlated well with both diffraction patterns. It is therefore suggested that  $\text{BH}_4^-$  can be substituted into the structure of  $\text{Li}_6\text{PS}_5\text{Br}$ .

Powder X-ray diffraction showed that  $\text{LB}_{0.33}\text{LPS}_{0.67}$  only contain  $\text{Li}_6\text{PS}_5\text{Br}$ , and it thereby also imply an absence of both hydrogen and boron in the crystal structure. The flat background of the diffractogram indicates that the sample is highly crystalline, and it seems unlikely that boron and hydrogen have become amorphous. A similar, but amorphous, system  $(\text{LiBH}_4)_x\text{LPS}_{(1-x)}$ , has been investigated [5], where it was suggested that the  $\text{BH}_4^-$  anions were incorporated into the amorphous structure after milling. Raman spectroscopy of the samples showed that the peak attributed to  $\text{BH}_4^-$  had disappeared for the mixed materials. In this work, the peak attributed to  $\text{BH}_4^-$  in infrared spectroscopy is still present in the samples where no crystalline  $\text{LiBH}_4$  is visible by diffraction. This substantiates the assertion that  $\text{BH}_4^-$  is present in the crystal structure of  $\text{Li}_6\text{PS}_5\text{Br}$ , and that it is not incorporated into the amorphous content.

The introduction of the new structure model resulted in a reduction of sulfur occupancies, which gives an increased number of vacancies in the structure. The structure model has only been tested for the  $\text{LB}_{0.33}\text{LPS}_{0.67}$  sample, as it is the only sample studied with PND.<sup>2</sup> Therefore, it is likely to believe that the structure model, and bromide occupancies, obtained from the other samples contain a systematic error, and that the refined occupancies would look different with the new structure model.

### Other factors

It was not possible to relate the conductivity values to the crystal structure of the materials, thus it seems that there are other features which

---

<sup>2</sup>The idea of  $\text{BH}_4^-$  substitution was first thought of late in the process, and it was therefore not enough time to measure PND for all samples. It is necessary to use PND to fully investigate the structures in these samples, as neutrons and X-rays are sensitive to different atomic properties

## 5.2. $LB_xLPS_{(1-x)}$ AS ELECTROLYTE MATERIAL

---

influence the conductivity.

An amorphous system of  $(LiBH_4)_xLPS_{(1-x)}$  has been investigated [5], where the samples showed ionic conductivities up to  $1.6 \cdot 10^{-3} \text{ S cm}^{-1}$  at room temperature. A study of the amorphous content indicated that the state of the  $BH_4^-$  anions were comparable to that of  $BH_4^-$  anions at the high temperature phase of  $LiBH_4$ . It is earlier claimed that the  $BH_4^-$  anions in HT- $LiBH_4$  are rotated, giving a delocalization of the negative charge, thus a weakened interaction between the  $Li^+$  and  $BH_4^-$  ions and an increased conductivity. One of the starting materials, LPS, is amorphous, and it is therefore probable that the samples contain amorphous phases. However, the samples with the highest backgrounds in their diffraction patterns are also the samples showing lowest conductivity values in this work. Thus, it seems more likely that the amorphous content contribute negatively to the ionic conductivities.

From the impedance measurements, it was observed that the two samples with highest conductivity values at room temperature,  $LB_{0.33}LPS_{0.67}$  and  $LB_{0.67}LPS_{0.33}$ , have the lowest grain boundary resistance.  $LB_{0.50}LPS_{0.50}$  showed highest grain boundary resistance at room temperature, but at elevated temperatures, it displayed similar values as the two samples mentioned above. The relation between conductivity, grain boundary resistance and particle size of a solid electrolyte material,  $Li_3OCl$ , have been investigated [29]. It was concluded that the conductivity of the material increased with increasing grain size, and that the activation energies for grain boundaries were higher compared to the activation energies of the bulk. If the grain size is small enough, the total conductivity will be dominated by conduction in the grain boundary. In this thesis, only bulk properties have been investigated when relating conductivity values to material properties. Depending on the size of the grains, the conduction of the lithium ions can be directly related to the grain boundary resistance.

## 5.2 $LB_xLPS_{(1-x)}$ as electrolyte material

One of the main issues with solid electrolytes is their low ionic conductivities at room temperature. Three of the samples in this thesis showed conductivity values in the range  $3-4 \cdot 10^{-3} \text{ S/cm}$  at 328 K, which is promising for appliances as solid electrolytes. From the three samples,  $LB_{0.33}LPS_{0.67}$  and  $LB_{0.50}LPS_{0.50}$ , were selected for battery tests and

cyclic voltammetry. Cyclic voltammetry showed that the materials are electrochemically stable up to 5 V, suggesting that they both have wide potential windows. Batteries with  $\text{LB}_{0.33}\text{LPS}_{0.67}$  as the electrolyte were cycled at  $\frac{C}{100}$  and  $\frac{C}{20}$ . The material is promising as an electrolyte material, as it shows repeatable cyclability at  $\frac{C}{20}$  and good stability towards the electrode material.

One major advantage with solid state batteries is that they can be used, and even perform better, at elevated temperatures. However, this requires the electrolyte materials to be stable in a wide temperature range. Thermoanalytical techniques, DSC and TGA, showed that the samples with highest conductivities are thermally stable up to at least 523 K.

### 5.3 Further work

Various structural features have been investigated in order to find a relation between sample content and conductivity, but it was not possible to find an absolute correlation. In this work, several features attribute at the same time, and it is therefore not possible to isolate their contribution. Each feature must be investigated separately to actually consider how it effect the conductivity of the material.

As one of the starting materials is amorphous, it is likely to believe that the samples contain amorphous phases. The results give a vague indication that the amorphous content contribute negatively to the conductivity values, and the amorphous content should be investigated.

In this work, only bulk properties have been investigated, while it is known that surface properties of materials affect the conductivity, such as the grain size. Therefore, also additional material properties should be investigated.

Introducing the new structure model altered the sulfur occupations in the structure, which again affects the number of vacancies in the structure. In order to investigate the crystal structure of the materials, all samples should be measured by neutron diffraction, and additional refinements may be performed from the new structure model.

To investigate how the materials function in actual batteries requires more thorough battery tests. Several batteries must be assembled, and cycled at different cycling rates for an abundant number of cycles.

### 5.3. FURTHER WORK

---

# Chapter 6

---

## Conclusion

The crystal structure and the electrochemical properties of the mixed  $\text{LiBH}_4\text{-LiBr-Li}_2\text{S-P}_2\text{S}_5$  system have been investigated. Electrochemical impedance spectroscopy showed that the samples exhibit ionic conductivities in the range  $10^{-4}$  -  $10^{-3}$   $\text{S cm}^{-1}$  at room temperature, and the highest conductivity value was measured in  $\text{LB}_{0.33}\text{LPS}_{0.67}$ ,  $1.1(7) \cdot 10^{-3}$   $\text{S/cm}$ .

The aim of the work has been to find a relation between the measured conductivities and the structure of the samples. Powder X-ray diffraction displayed that the  $\text{Li}_6\text{PS}_5\text{Br}$  phase was formed in all samples, while the high-temperature phase of  $(\text{LiBH}_4)_{(1-y)}\text{Br}_y$  was found in three out of the five samples. A thorough investigation of the structural properties for each sample was executed, and properties such as phase content, bromide occupations, unit cell volumes, anion displacement and temperature factors were tried related to the conductivity. However, no obvious correlation was found between sample content and conductivity values.

The  $\text{Li}_6\text{PS}_5\text{Br}$  phase was investigated in  $\text{LB}_{0.33}\text{LPS}_{0.67}$  by powder neutron diffraction, and the results revealed that the structure model obtained from PXD did not match the data obtained from PND. A new structure model was constructed, where sulfur could be substituted by both bromide and borohydride at the substitutional sites, and the new structure model correlated well with both diffractograms. It is therefore suggested that borohydride can be substituted into the structure of  $\text{Li}_{7-x-y}\text{PS}_{6-x-y}\text{Br}_x(\text{BH}_4)_z$ . The refined occupations from the new struc-

---

ture model are altered compared to the original model. As the original structure model is used in the refinements of all of the samples, it is expected that the structural information contain systematic errors.

Electrochemical properties of  $\text{LB}_{0.33}\text{LPS}_{0.67}$  and  $\text{LB}_{0.50}\text{LPS}_{0.50}$  were investigated by cyclic voltammetry and battery cycling. Cyclic voltammetry showed that the electrolyte materials are electrochemically stable up to 5 V, suggesting that they have wide potential windows. The results from battery cycling imply that the  $\text{LB}_{0.33}\text{LPS}_{0.67}$  material is promising as electrolyte material, as it shows repeatable cyclability at  $\frac{C}{20}$  and good stability towards the electrode material.

---

# Bibliography

- [1] D.W.Zhou L.Wan C.Lia, P.Peng. Research progress in libh4 for hydrogen storage: A review. *International Journal of Hydrogen Energy*, 2011.
- [2] Hitoshi Takamura Mariko Ando Yasuto Noda Taiki Karahashi Shin-ichi Orimo Hideki Haekawa, Motoaki Matsuo. Halide-stabilized libh4, a room-temperature lithium fast-ion conductor. *JACS*, 2009.
- [3] Hideki Maekawa Hai-Wen Li Shin-ichi Orimo Motoaki Matsuo, Hitoshi Takamura. Stabilization of lithium superionic conduction phase and enhancement of conductivity of libh4 by licl additon. *Applied physics letters*, 2009.
- [4] Jiho Lee Dongwook Shin Lunghoon Kim, Youngsub Yoon. Formation of the high lithium ion conducting phase from mechanically milled amorphous  $\text{li}_2\text{s-p}_2\text{s}_5$ . *Journal of power sources*, 2010.
- [5] Akitoshi Hayashi Masahiro Tatsumisago Akihiro Yamauchi, Atsushi Sakuda. Preparation and ionic conductivities of  $(100 - x)(0,75 \text{ li}_2\text{s} \cdot 0,25\text{p}_2\text{s}_5) \cdot x\text{libh}_4$  glass electrolyte. *Journal of power sources*, 2012.
- [6] Terrence J Udovic Motoaki Matsuo Tamio Ikeshoji Shin-ichi Orimo. Atsushi Unemoto, Hui Wu. Fast lithium-ionic conduction in a nex complex hydride-sulphide crystalline phase. *Royal Society of Chemistry*, 2016.
- [7] Yudong Gong David P. Wilkinson JiuJun Zhang Chunwen Sun, Jin Liu. Recent advances i all-solid-state rechargable lithium batteries. *Nano Energy*, 2017.

## BIBLIOGRAPHY

---

- [8] Stephen Elliot. The physics and chemistry of solids. *Wiley*, 2006.
- [9] Anthony West John Irvine, Derek Sinclair. Electroceramics: Characterization by impedance spectroscopy. *Advanced materials*, 1990.
- [10] Sigita Trabesinger Petr Novak Lorentz Gubler Renaud Bouchet. Joanna Conder, Claire Villevieille. Electrochemical impedance spectroscopy of a li-s battery: Part 1. influence of the electrode and electrolyte composition on the impedance of symmetric cells. *Electrochimica Acta*, 2017.
- [11] K. Steiner Ch. Wimmer T. Soczka-Guth D.U. Sauer. D. Andre, M. Meiler. Charecterization of high-power-lithium batteries by electrochemical impedance spectroscopy.i.experimental investigation. *Journal of Power sources*, 2011.
- [12] Gamry instruments. Basics of electrochemical impedance spectroscopy. <https://www.gamry.com/application-notes/EIS/basics-of-electrochemical-impedance-spectroscopy/>.
- [13] Peter Y. Zavalij Vitalij K. Pecharsky. Fundamentals of powder diffraction and structural characterization of materials. *Springer*, 2005.
- [14] G. Artioli D. Viterbo M.Milanesio G.Ferraris-G. Gilli P.Gilli G.Zanotti M.Catti C. Giacobozzo, H.L. Monaco. Fundamentals of crystallography. *Oxford Science Publications, Third edition*, 2011.
- [15] Roger Pynn. An introduction to neutron scattering. [https://neutrons.ornl.gov/sites/default/files/intro\\_ton\\_neutron\\_scattering.pdf](https://neutrons.ornl.gov/sites/default/files/intro_ton_neutron_scattering.pdf). [Online; accessed 12-05-18].
- [16] B. T. M. Willis A. Albinati. The rietveld method in neutron and x-ray powder diffraction. *International Union of Crystallography*, 1982.
- [17] Barbara Stuart. *Infrared spectroscopy: fundamentals and applications*. John Wiley and Sons, 2004.
- [18] Chapter 4: Group Theory. [https://www.ethz.ch/content/dam/ethz/special\\_interest/chab/physical\\_chemistry/ultrafast\\_spectroscopy](https://www.ethz.ch/content/dam/ethz/special_interest/chab/physical_chemistry/ultrafast_spectroscopy) –



- dam/documents/lectures/spectroscopyFS13/scriptFS13/PCVch4.pdf*.  
[Online; accessed 12-05-18].
- [19] K. Nakamoto. *Infrared and Raman Spectra of Inorganic and Coordination Compound*. Wiley, 2009.
- [20] Brian D. McCarthy Eric S. Rountree Thomas T. Eisenhart Noemie Elgrishi, Kelley J. Rountree and Jillian L. Dempsey. A practical beginner's guide to cyclic voltammetry. *Journal of chemical education*, 2017.
- [21] Craig E. Banks Dale A. C. Brownson. *The handbook of graphene electrochemistry*. Springer, 2014.
- [22] Magnus Moe Nygård. The influence of iron on the structure and properties of ti-v based metal hydrides. *Master thesis*, 2017.
- [23] Michael Haynes Steve W. Martin Christian Bischoff, Katherine Schuller. Structural investigations of  $\text{yna}_2 + (1-y)\text{ps}_2/5$  glasses using raman spectroscopy and infrared spectroscopies. *Journal of non-crystalline solids*, 2012.
- [24] Koji Yoshida Ponniah Vajeeston Sangryun Kim Magnus H.Sørby Shin-ichi Orimoc Helmer Fjellvåg Bjørn C.Hauback Abdelouahab Elkharchachi, Yang Hu. Lithium ionic conduction in composites of  $\text{li}(\text{bh}_4)_{0.75}\text{i}_{0.25}$  and amorphous  $0.75\text{li}_2\text{s}\cdot 0.25\text{p}_2\text{s}_5$  for battery applications. *Electrochimica Acta*, 2018.
- [25] Michael Haynes Steve Martin Christian Bischoff, Katherine Schuller. Structural investigation of  $\text{yna}_2\text{s} + (1-y)\text{ps}_2/5$  glasses using raman and infrared spectroscopies. *Journal of Non-Crystalline Solids*, 2012.
- [26] Edmund Cussen Duncan Gregory Irene Cascallana-Matias, David Keen. Phase behavior in the  $\text{libh}_4\text{-libr}$  system and structure of the anion-stabilized fast ionic, high temperature phase. *Chemistry of Materials*, 2015.
- [27] Eckert H Vabbahme J Reiner C. Zaiss T. Schlosser M. Deiseroth HJ, Kong ST.  $\text{Li}_6\text{ps}_5\text{cl}$ : A class of crystalline li-rich solids with an unusually high ionic  $\text{li}^+$  mobility. *Angewandte Chemie*, 2008.

## BIBLIOGRAPHY

---

- [28] Marnix Wagemaker Niek J.J. de Klerk, Irek Roslon. Diffusion mechanism of li argyrodite solid electrolyter for li-ion batteries and prediction of optimized halogen doping: The effect of li vacancies, halogens, and halogen disorder. *Chemistry of Materials*, 2016.
- [29] Theodosios Famprikis Christian Masquelier James A. Dawson, Pieremanuele Canepa and M. Saiful Islam\*. Atomic-scale influence of grain boundaries on li-ion conduction in solid electrolytes for all-solid-state batteries. *Journal of the Maerican chemical society*, 2018.
- [30] Alessandro Damin Giuseppe Spoto Piero Ugliengo Marcello Baricio Olena Zavortynska, Marta Corno. Vibrational properties of mbh<sub>4</sub> ans mbf<sub>4</sub> crystals (m=li,na,k): A combined dft, infrared and raman study. *The journal of Physical Chemistry*, 2011.
- [31] Zavorotynska L.M. Arnbjerg D.B. Ravnsbæk R.A. Malmkjær H. Grove B.C. Hauback M. Baricco Y. Filinchuk F. Besenbacher T.R. Jensen L.H. Rude, O. Bromide substitution in lithium borohydride, libh<sub>4</sub>-libr. *International Journal of Hydrogen Energy*, 2011.

# Appendix A

---

## Impedance measurements

### A.1 Uncertainty in the impedance measurements

$$\sigma(r, d, R) = \frac{d}{R_{tot}\pi r^2}$$

$$\Delta\sigma(x_1, x_2, \dots) = \sqrt{\left(\frac{\partial\sigma}{\partial x_1} \cdot \Delta x_1\right)^2 + \left(\frac{\partial\sigma}{\partial x_2} \cdot \Delta x_2\right)^2 + \dots} \quad (\text{A.1})$$

$$\frac{\partial\sigma}{\partial d} = \frac{1}{\pi r^2 R} = \frac{\sigma}{d}$$

$$\frac{\partial\sigma}{\partial r} = \frac{-2d}{\pi r^3 R} = \frac{-2\sigma}{r}$$

$$\frac{\partial\sigma}{\partial R} = \frac{-d}{\pi r^2 R^2} = \frac{-\sigma}{R}$$

$$\frac{\Delta\sigma}{\sigma} = \sqrt{\left(\frac{\Delta d}{d}\right)^2 + \left(\frac{-2\Delta r}{r}\right)^2 + \left(\frac{-\Delta R}{R}\right)^2} \quad (\text{A.2})$$

## A.2. NYQUIST PLOTS OF ALL SAMPLES

Sample	d [cm]	$\Delta d$ [cm]	R [ $\Omega$ ]	$\Delta R$ [ $\Omega$ ]	r [cm]	$\Delta r$ [cm]	$\frac{\Delta\sigma}{\sigma}$
x = 0.25	0.167	0.002	510	15.3	0.5	0.002	0.0613
x = 0.33	0.165	0.002	192	5.8	0.5	0.002	0.0618
x = 0.50	0.167	0.002	300	9	0.5	0.002	0.0613
x = 0.67	0.166	0.002	220	6.6	0.5	0.002	0.0613
x = 0.75	0.169	0.002	560	17	0.5	0.002	0.0619

Table A.1: Calculated uncertainties for the impedance measurements of the different samples.

## A.2 Nyquist plots of all samples

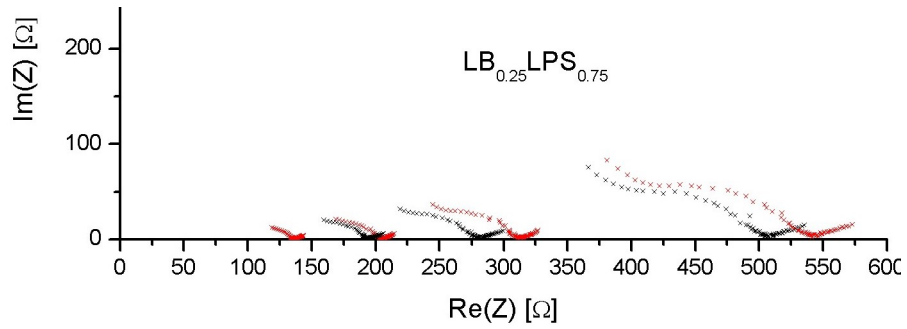


Figure A.1: Impedance plot for LB<sub>0.25</sub>LPS<sub>0.75</sub>, where red is measurements obtained during heating and black during cooling.

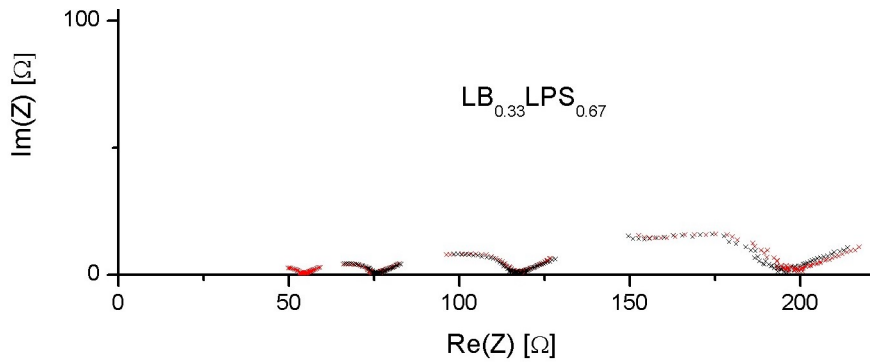


Figure A.2: Impedance plot for LB<sub>0.33</sub>LPS<sub>0.67</sub>, where red is measurements obtained during heating and black during cooling.

APPENDIX A. IMPEDANCE MEASUREMENTS

---

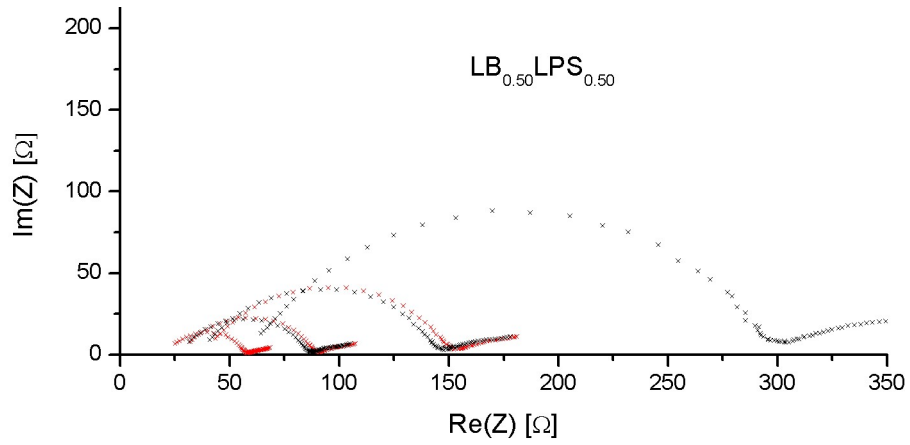


Figure A.3: Impedance plot for  $\text{LB}_{0.50}\text{LPS}_{0.50}$ , where red is measurements obtained during heating and black during cooling.

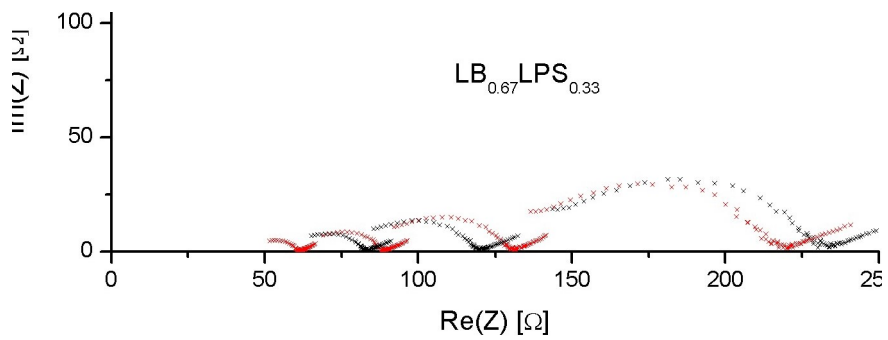


Figure A.4: Impedance plot for  $\text{LB}_{0.67}\text{LPS}_{0.33}$ , where red is measurements obtained during heating and black during cooling.

## A.2. NYQUIST PLOTS OF ALL SAMPLES

---

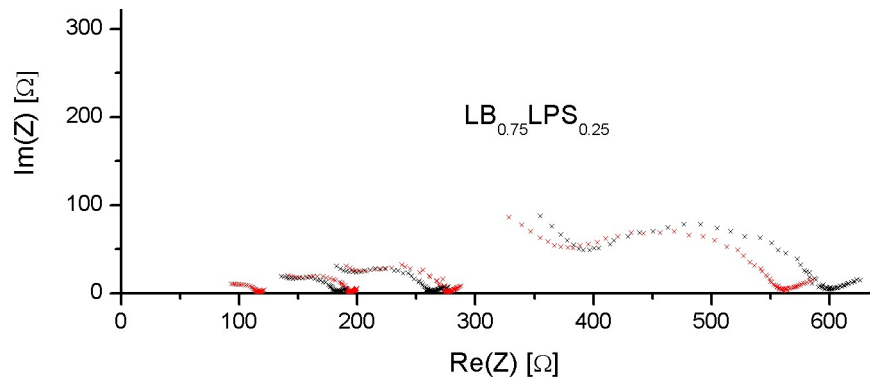


Figure A.5: Impedance plot for  $\text{LB}_{0.75}\text{LPS}_{0.25}$ , where red is measurements obtained during heating and black during cooling.

# Appendix B

---

## Structural analysis

### B.1 Infrared spectroscopy

The two following sections are based on the work done by Zavortynska et al [30] and Rude et al [31].

#### B.1.1 LiBH<sub>4</sub>

The free BH<sub>4</sub><sup>-</sup> anion belong to the symmetry group T<sub>d</sub>. It has 4 vibrational modes,  $\tilde{\nu}_1(A_1)$ ,  $\tilde{\nu}_2(E)$ ,  $\tilde{\nu}_3(F_2)$  and  $\tilde{\nu}_4(F_2)$ , shown in table B.1, where only  $\tilde{\nu}_3(F_2)$  and  $\tilde{\nu}_4(F_2)$  are IR-active. When BH<sub>4</sub><sup>-</sup> is positioned in a crystal, the symmetry of the anion will change due to site symmetry and crystal field effects. In LiBH<sub>4</sub> the T<sub>d</sub> symmetry group of BH<sub>4</sub> is reduced to C<sub>s</sub> site symmetry. This reduction leads to a splitting of the degenerate modes,  $\tilde{\nu}_2(E)$ ,  $\tilde{\nu}_3(F_2)$  and  $\tilde{\nu}_4(F_2)$ . The species are transformed into the symmetry species of the D<sub>2h</sub> group, which is described in table B.2. The modes with subscript u indicates that the transforming function is even under inversion, and these modes are IR-active. This means that the B<sub>1u</sub>, B<sub>2u</sub> and B<sub>3u</sub> may appear in the IR-spectra. Combining this with the  $\tilde{\nu}_1(A_1)$ ,  $\tilde{\nu}_2(E)$ ,  $\tilde{\nu}_3(F_2)$  and  $\tilde{\nu}_4(F_2)$  gives the possible theoretical modes given in table B.3. The table shows both theoretically calculated infrared modes, modes that are experimentally found by others and the modes that are found in this thesis. From the table it is clear that the modes

### B.1. INFRARED SPECTROSCOPY

---

found in this thesis matches well with the expected values. Figure B.1 shows the measured infrared spectra of  $\text{LiBH}_4$ , where the modes have been assigned to the peaks.

Point group	Total number of atoms	Species	Number of vibrations
$T_d$	$24m + 12m_d + 6m_2 + 4m_3 + m_0$	$A_1$	$3m + 2m_d + m_2 + m_3 = 0 + 0 + 0 + 1 = 1$
		$A_2$	$3m + m_d = 0 + 0 = 0$
		$E$	$6m + 3m_d + m_2 + m_3 = 0 + 0 + 0 + 1 = 1$
		$F_1$	$9m + 4m_d + 2m_2 + m_3 - 1 = 0 + 0 + 0 + 1 - 1 = 0$
		$F_2$	$9m + 5m_d + 3m_2 + 2m_3 + m_0 - 1 = 0 + 0 + 0 + 0 + 2 \cdot 1 + 1 - 1 = 2$

Table B.1:  $m_0$  sets of nuclei on all elements of symmetry,  $m_d$  sets of nuclei in the mirror plane,  $m_{2,3,4}$  sets of nuclei on a 2,3,4-fold axes of rotation,  $m$  - sets of nuclei not on any elements of symmetry.

$\tilde{\nu}_1(A_1)$	$A'$	$B_{1u}, B_{3u}$
$\tilde{\nu}_2(E)$	$A' + A''$	$B_{1u}, B_{3u}, B_{2u}$
$\tilde{\nu}_3(F_2)$	$2A' + A''$	$B_{1u}, B_{3u}, B_{1u}, B_{3u}, B_{2u}$
$\tilde{\nu}_4(F_2)$	$2A' + A''$	$B_{1u}, B_{3u}, B_{1u}, B_{3u}, B_{2u}$

Table B.2: Splitting of normal modes of  $T_d$  symmetry to  $C_s$  symmetry, giving the possible IR modes for  $\text{LiBH}_4$



Mode	Calculated	Experimentally found	Found in thesis
$\tilde{\nu}_3, A' - B_{3u}$	2393	2300	2300
$\tilde{\nu}_3, A'' - B_{2u}$	2389	2270	2272
$\tilde{\nu}_2, A' - B_{3u}$	1316	1307	1308
$\tilde{\nu}_2, A'' - B_{2u}$	1285	1285	1287
$\tilde{\nu}_4, A' - B_{1u}$	1246	1232	1232
$\tilde{\nu}_4, A'' - B_{2u}$	1064	1089	1091

Table B.3: The table shows the expected modes from infrared spectroscopy of  $\text{LiBH}_4$  with corresponding wavenumber. The first column gives theoretically calculated modes, the second column gives modes that are experimentally found [30], and the last column gives the modes found in this thesis

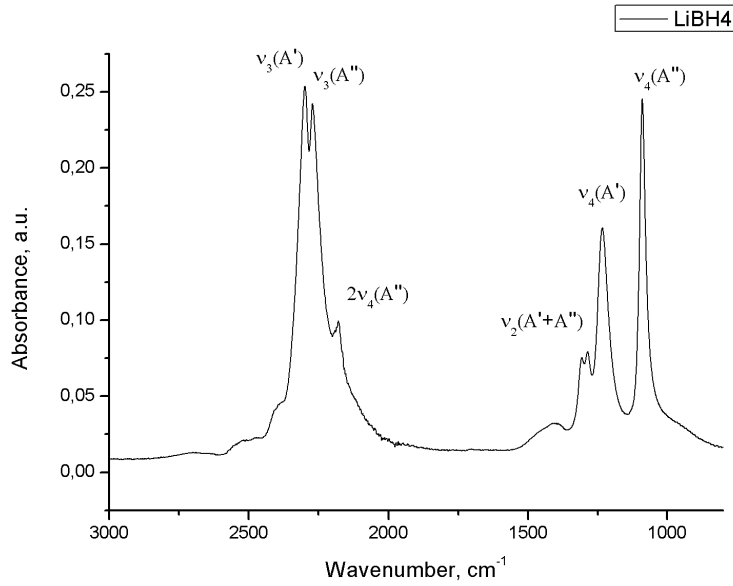


Figure B.1: Infrared spectrum obtained from  $\text{LiBH}_4$  sample, where the peaks have been assigned to modes.

### B.1.2 LB

Figure B.2 shows a comparison between the infrared spectra obtained from  $\text{LiBH}_4$  and LB. In the orthorhombic phase of  $\text{LiBH}_4$ ,  $\text{BH}_4^-$  has  $C_s$

## B.2. POWDER X-RAY DIFFRACTION

---

site symmetry, while it in the hexagonal phase has  $C_{3v}$  site symmetry [31]. This change in symmetry reduces the degeneracy of the  $\tilde{\nu}_3$  from three to two, and this reduction may be observed in the figure by a smeared out peak at around  $2300\text{ cm}^{-1}$ . The peaks in the bending region are also affected by the substitution, and it seems as they are smeared out. This makes it difficult to say whether the peaks have been shifted, disappeared or if any new modes have been formed. However, in the spectrum obtained from  $\text{LiBH}_4$  there is a clear gap between the  $\tilde{\nu}_4(A')$  and  $\tilde{\nu}_4(A'')$  modes, which is not present in the LB-spectra, and it may be that a new peak has appeared around this wavenumber. Also, the broad peak at around  $1400\text{ cm}^{-1}$  in the  $\text{LiBH}_4$  spectra has disappeared in the LB spectra.

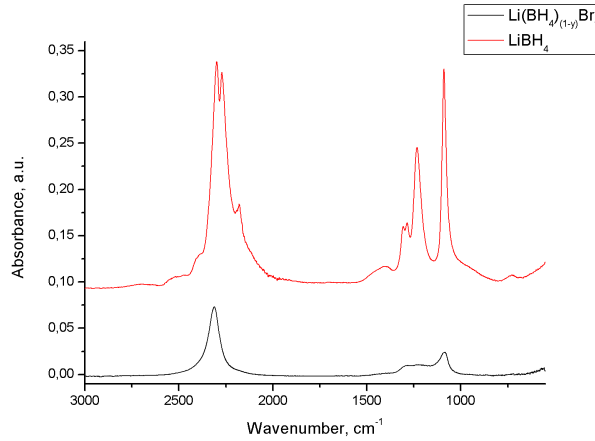


Figure B.2: Comparison of infrared spectra obtained from  $\text{LiBH}_4$  and LB.

## B.2 Powder X-ray diffraction

### B.2.1 Stabilization of HT- $\text{LiBH}_4$ by halide substitution

The goal of milling and annealing  $2\text{LiBH}_4 + \text{LiBr}$  was to obtain a solid solution of the hexagonal phase of  $\text{Li}(\text{BH}_4)_{0.67}\text{Br}_{0.33}$  at room temperature. The EVA software was used for phase identification by matching the observed Bragg peaks to phases containing Li, B, H and/or Br in the

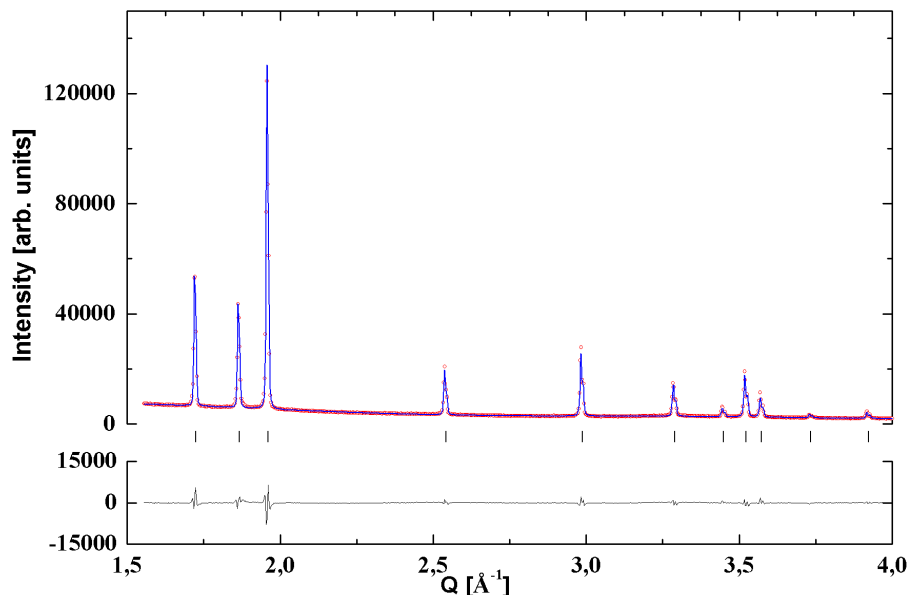


Figure B.3: Rietveld fit to the PXD data of the annealed sample of LB.

PDF-4 database, and the HT-phase of  $\text{LiBH}_4$  alone was found as the best candidate in the samples. The crystal structures of the samples were further investigated by Rietveld refinements in TOPAS. The refinements were based on the structure of HT- $\text{LiBH}_4$ , where a bromide ion was placed at the same site as the boron ion, and the sum of their occupancies were constrained to one. Two samples with the same milling conditions were investigated, whereas one of the samples was annealed at  $150\text{ }^\circ\text{C}$  for 14 hours. The diffraction patterns of the two samples are shown in figure B.3 and B.4, and they show that neither the orthorhombic  $\text{LiBH}_4$  phase nor the  $\text{LiBr}$  phase are present in the samples. This indicates that a significantly amount of bromide is substituted into  $\text{LiBH}_4$  after ball milling, and that ball milling alone is enough to produce a solid solution of the materials and to stabilize the hexagonal structure at room temperature.

Table B.4 shows that the occupancy of bromide was refined to approximately 40 % for the as-milled sample and 46 % for the annealed one. The occupancy of bromide was expected to be 33%, and the refined values exceed this number for both samples. The  $\text{LiBH}_4$  phase contains originally only light scatterers with low atomic numbers. As the heavy

## B.2. POWDER X-RAY DIFFRACTION

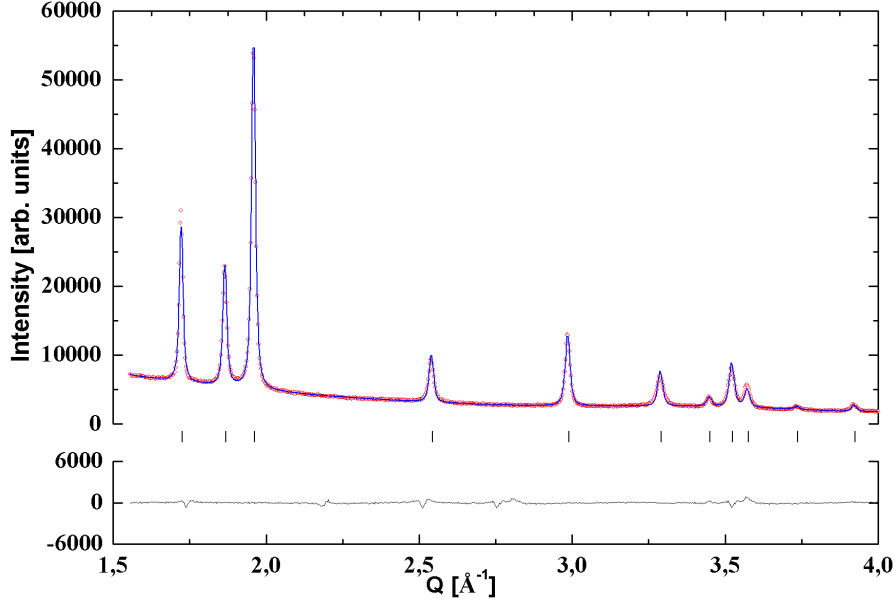


Figure B.4: Rietveld fit to the PXD data of the as-milled sample of LB.

bromide, atomic number 35, is introduced into the structure, it will tend to dominate the x-ray scattering of the structure. The diffractograms in figures B.3 and B.4 show that neither orthorhombic  $\text{LiBH}_4$  nor the  $\text{LiBr}$  are present in the samples, and the flat background in the diffractograms indicate that the samples are highly crystalline. Due to this, it is suggested that the starting materials are fully reacted and that  $\text{Li}(\text{BH}_4)_{0.67}\text{Br}_{0.33}$  is formed.

Table B.4 shows that the bromide and borohydride in the as-milled and annealed samples are displaced by  $0.118 \text{ \AA}$  and  $0.135 \text{ \AA}$  respectively.

	Unit cell volume [ $\text{\AA}^3$ ]	Z-position, $\text{BH}_4$	Z-position, Br	Bromide occupancy	Temperature factors[]
As-milled	102.69(3)	0.697(2)	0.579(9)	0.40(3)	4.3(5)
Annealed	103.12(2)	0.706(5)	0.571(3)	0.46(1)	2.8(2)
Reference	110.04	0.553(1)			8.6(4)

Table B.4: Structural properties of the as-milled and annealed LB samples obtained from TOPAS.

## B.3 Powder neutron diffraction

### B.3.1 Misfit of structure model

The diffractogram obtained from the deuterated  $\text{LB}_{0.33}\text{LPS}_{0.67}$  sample is given in figure B.5.

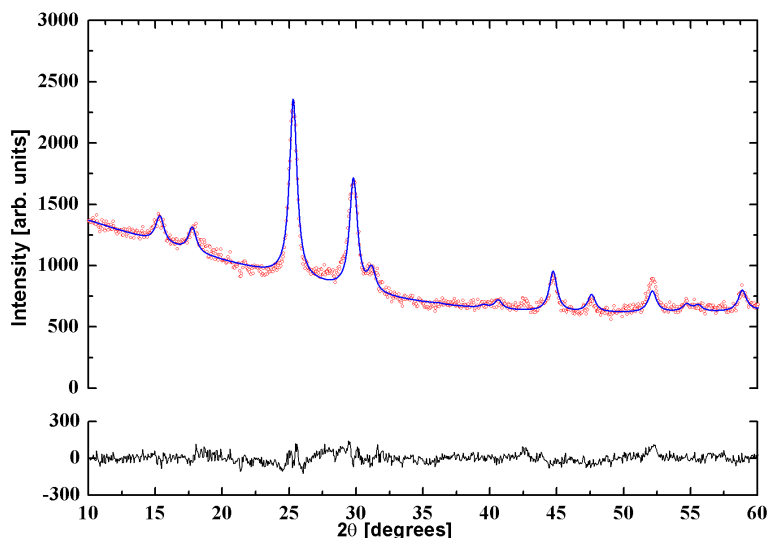


Figure B.5: Rietveld fit to the PND data of the deuterated sample of  $\text{LB}_{0.33}\text{LPS}_{0.67}$

To investigate how the amount of substituted bromide influence the diffraction pattern, the refined occupancies from X-ray diffraction were inserted into the structure model for the neutron sample and vice versa. The calculated and measured diffraction patterns for the samples are shown in figures B.6 and B.7, and it is obvious from the figures that the structure model obtained from X-ray diffraction does not fit the data from neutron diffraction. This indicates that the structure model used in the refinements, does not fit for both techniques. Neutron and X-ray diffraction are sensitive to different atomic properties, and the same change in crystal structure can affect the diffraction pattern quite differently. It was therefore desirable to find a structure model that fit the structures obtained from both techniques.

### B.3. POWDER NEUTRON DIFFRACTION

---

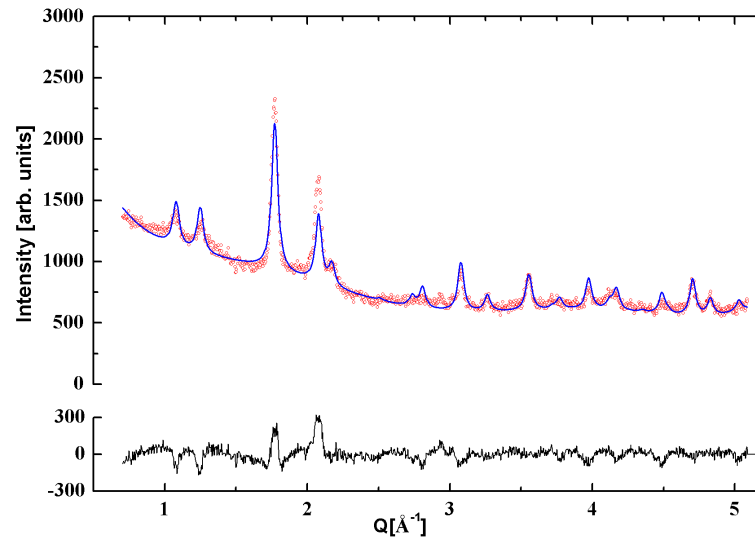


Figure B.6: SR-PXD data fitted with structure model obtained from PND refinements.

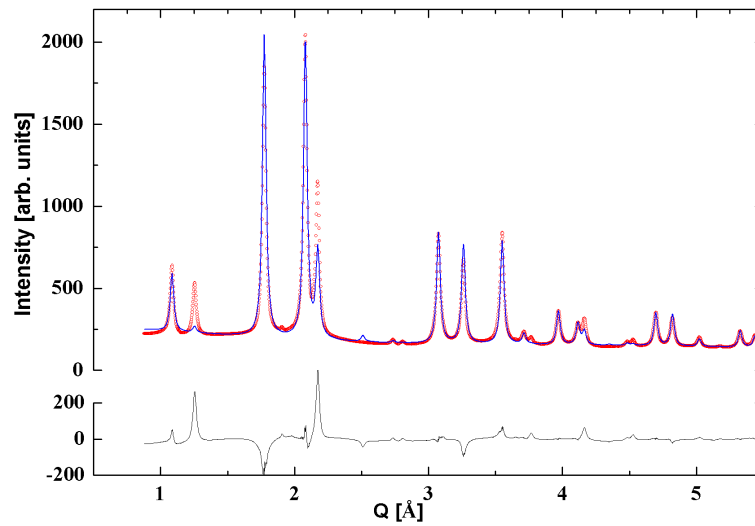


Figure B.7: PND data fitted with structure model obtained from SR-PXD refinements.

### B.3.2 Difference in PND sample and SR-PXD sample

The  $\text{LB}_{0.33}\text{LPS}_{0.67}$  sample for PND was synthesized with  ${}^7\text{Li}$ ,  ${}^{11}\text{B}^2$  and  $\text{D}$ , and it is therefore not the same sample measured at the synchrotron facility and with neutron diffraction. They are synthesized under the same conditions, but that does not guarantee that the resultant samples are equal. X-ray diffraction of the sample made for neutron diffraction showed that the bromide occupancies were refined to higher values,  $\text{occ}_{4a} = 0.46$  and  $\text{occ}_{4d} = 0.32$ , than found from the synchrotron sample,  $\text{occ}_{4a} = 0.33$  and  $\text{occ}_{4d} = 0.22$ . Synchrotron radiation gives much better statistics, and the occupational difference could be explained by this. However, it is likely to believe that the samples are slightly different, and a perfect match between the neutron and x-ray diffraction patterns will therefore not be possible. The x-ray diffraction pattern of the neutron sample obtained from the homelab is shown in figure B.8. It shows that the structure model fits the measured diffraction patterns quite well, suggesting that the structure model give a good fit for all of the samples.

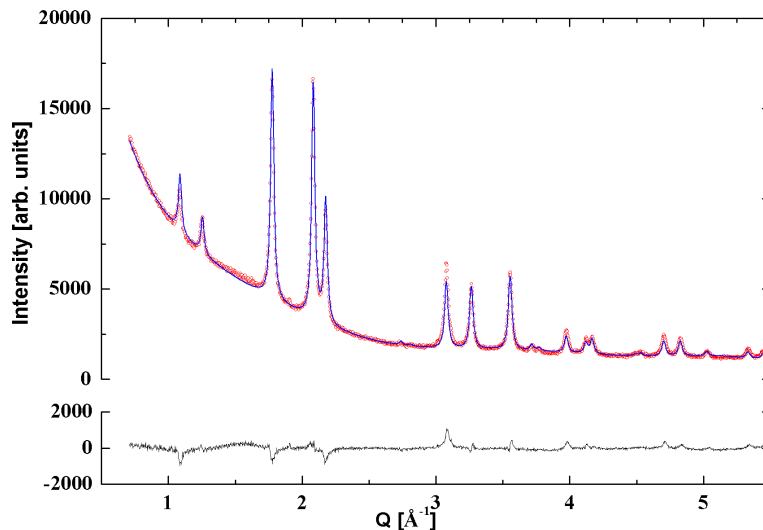


Figure B.8: PXD data of the neutron sample fitted with structure model obtained from combined refinements.

### B.3.3 Neutron diffraction of LPS sample

The diffractogram of the deuterated sample of  $\text{LB}_{0.33}\text{LPS}_{0.67}$  has a high background, with some distinct Bragg peaks visible. To investigate the source of the noise, the LPS-material was also studied by neutron diffraction. Its diffraction pattern, B.9, showed no distinct Bragg peaks and a high background signal, and it is therefore suggested that the noise measured in the  $\text{LB}_{0.33}\text{LPS}_{0.67}$  sample comes from the LPS material.

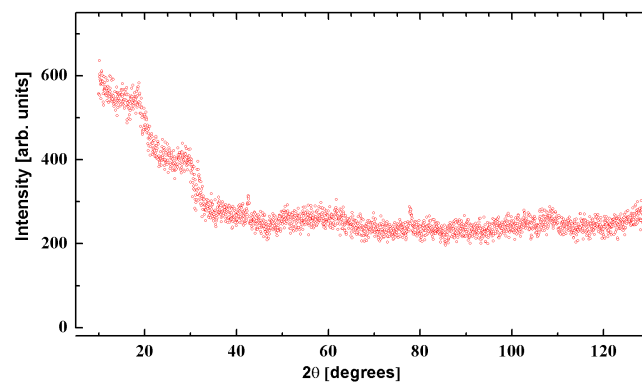


Figure B.9: Neutron diffraction pattern form LPS sample.



# Appendix C

---

## Properties for electrolyte materials

### C.1 Thermal analyses

#### C.1.1 Diffractogram of heat treated $\text{LB}_{0.25}\text{LPS}_{0.75}$

An exothermic event was observed in the samples, and to investigate whether the event is connected to a recrystallization of the samples, the  $\text{LB}_{0.75}\text{LPS}_{0.25}$  was heat treated up to 300 °C before it was measured with X-ray diffraction. The diffractogram clearly shows that the sample is recrystallized, and no trace of the earlier identified phases is visible. Using the Eva software, LiBr and  $\text{Li}_2\text{S}$  are identified, but several more peaks remain unidentified. The diffractogram is shown in figure C.1

C.1. THERMAL ANALYSES

---

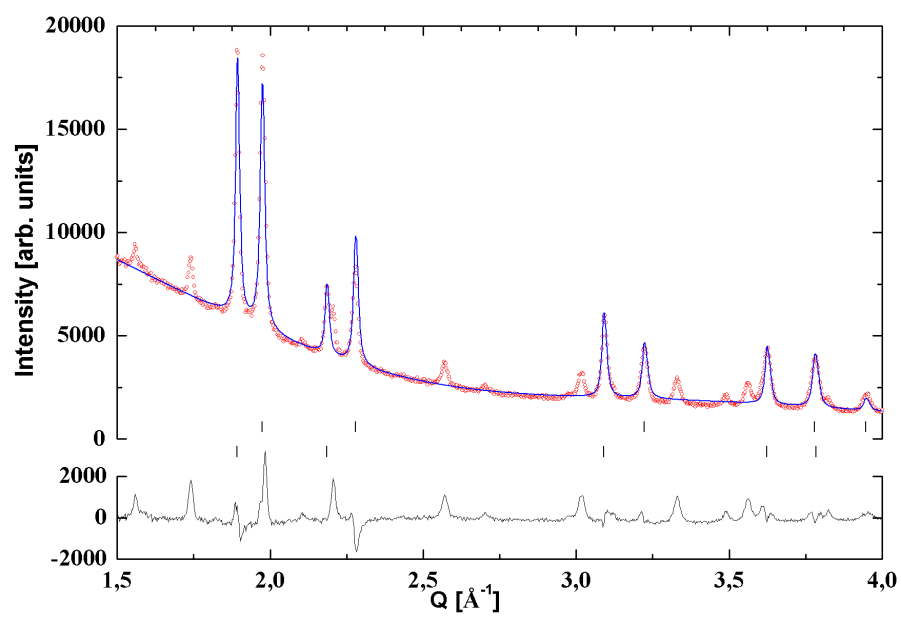


Figure C.1: Diffraction pattern of the recrystallized sample

### C.1.2 TGA

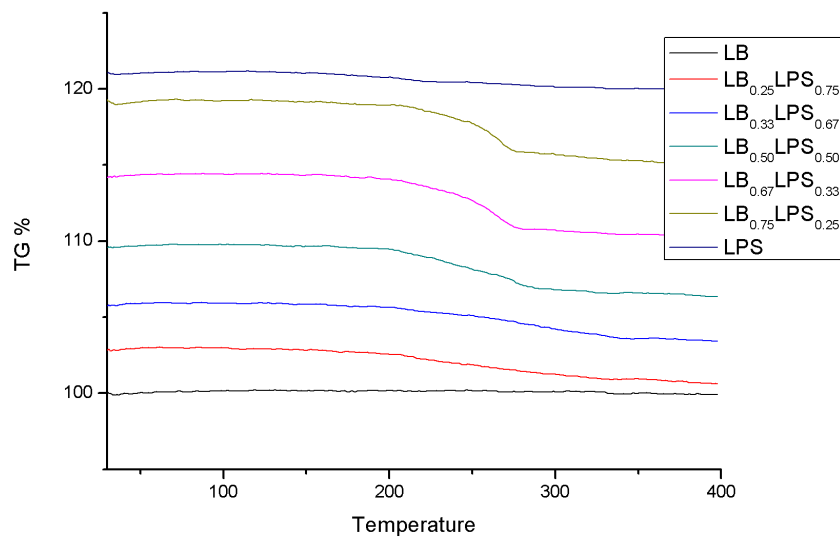


Figure C.2: Massloss in the samples

### C.2 Cycling of LB<sub>0.50</sub>LPS<sub>0.50</sub>

C.2. CYCLING OF  $LB_{0.50}LPS_{0.50}$

---

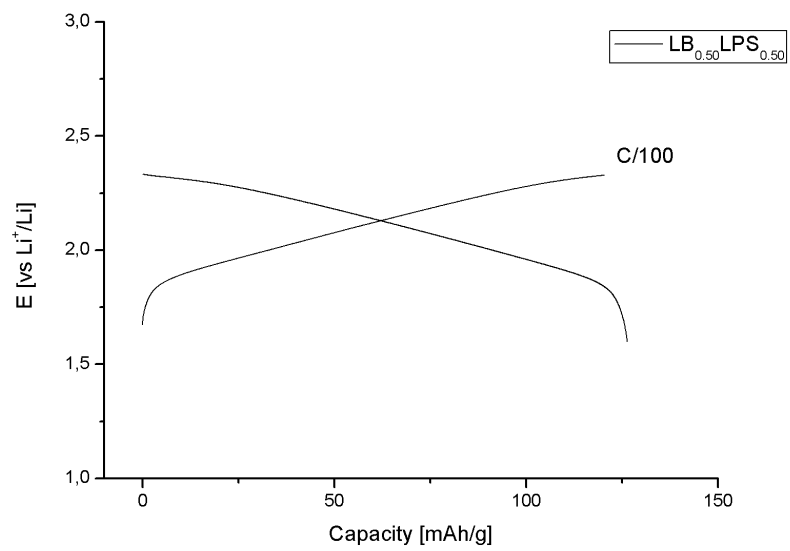


Figure C.3: Incomplete battery cycle of  $LB_{0.50}LPS_{0.50}$